Systems genetics analyses in Diversity Outbred mice inform human bone mineral density GWAS and identify *Qsox1* as a novel determinant of bone strength

Basel M. Al-Barghouthi[1,2,8], Larry D. Mesner[1,6,8], Gina M. Calabrese[1,8], Daniel Brooks[3], Steven M. Tommasini[4], Mary L. Bouxsein[3], Mark C. Horowitz[4], Clifford J. Rosen[5], Kevin Nguyen[1], Samuel Haddox[2], Emily A. Farber[1], Suna Onengut-Gumuscu[1,6], Daniel Pomp[7] and Charles R. Farber[1,2,6]

[1] Center for Public Health Genomics, School of Medicine, University of Virginia, Charlottesville, VA 22908
[2] Department of Biochemistry and Molecular Genetics, School of Medicine, University of Virginia, Charlottesville, VA 22908
[3] Center for Advanced Orthopedic Studies, Beth Israel Deaconess Medical Center, Department of Orthopedic Surgery, Harvard Medical School, Boston, MA 02215
[4] Department of Orthopaedics and Rehabilitation, Yale School of Medicine, New Haven, CT 06520
[5] Maine Medical Center Research Institute, 81 Research Drive, Scarborough, ME 04074
[6] Department of Public Health Sciences, School of Medicine, University of Virginia, Charlottesville, VA 22908
[7] Department of Genetics, University of North Carolina School of Medicine, Chapel Hill, NC 27599
[8] Contributed equally to this work

Correspondence to:

Charles R. Farber
E-mail: crf2s@virginia.edu
Center for Public Health Genomics
University of Virginia
P.O. Box 800717
Charlottesville, VA 22908, USA
Tel. 434-243-8584

ABSTRACT:

Genome-wide association studies (GWASs) for osteoporotic traits have identified over 1000 associations; however, their impact has been limited by the difficulties of causal gene identification and a strict focus on bone mineral density (BMD). Here, we used Diversity Outbred (DO) mice to directly address these limitations by performing the first systems genetics analysis of 55 complex skeletal phenotypes. We applied a network approach to cortical bone RNA-seq data to discover 72 genes likely to be causal for human BMD GWAS associations, including the novel genes *SERTAD4* and *GLT8D2*. We also performed GWAS in the DO for a wide-range of bone traits and identified *Qsox1* as a novel gene influencing cortical bone accrual and bone strength. Our results provide a new perspective on the genetics of osteoporosis and highlight the ability of the mouse to inform human genetics.

52 **INTRODUCTION:**

53 Osteoporosis is a condition of low bone strength and an increased risk of fracture [1]. It is
54 also one of the most prevalent diseases in the U.S., affecting over 10 million
55 individuals[2]. Over the last decade, efforts to dissect the genetic basis of osteoporosis
56 using genome-wide association studies (GWASs) of bone mineral density (BMD) have
57 been tremendously successful, identifying over 1000 independent associations [3–5].
58 These data have the potential to revolutionize our understanding of bone biology and
59 discovery of novel therapeutic targets [6,7]; however, progress to date has been limited.
60

61 One of the main limitations of human BMD GWAS is the difficulty identifying causal
62 genes. This is largely due to the fact that most associations implicate non-coding
63 variation presumably influencing BMD by altering gene regulation [5]. For other diseases,
64 the use of molecular "-omics" data (*e.g.*, transcriptomic, epigenomic, etc.) in conjunction
65 with systems genetics approaches (*e.g.*, identification of expression quantitative trait loci
66 (eQTL) and network-based approaches) has successfully informed gene discovery [8,9].
67 However, few "-omics" datasets exist on bone or bone cells in large human cohorts (*e.g*,
68 bone or bone cells were not part of the Gene Tissue Expression (GTEx) project [10]),
69 limiting the use of systems genetics approaches to inform BMD GWAS [11].
70

71 A second limitation is that all large-scale GWASs have focused exclusively on BMD [3–5].
72 BMD is a clinically relevant predictor of osteoporotic fracture; however, it explains only
73 part of the variance in bone strength [12–15]. Imaging modalities and bone biopsies can be
74 used to collect data on other bone traits such as trabecular microarchitecture and bone

formation rates; however, it will be difficult to apply these techniques “at scale” (N=>100K). Additionally, many aspects of bone, including biomechanical properties, cannot be measured *in vivo*. These limitations have hampered the dissection of the genetics of osteoporosis and highlight the need for resources and approaches that address the challenges faced by human studies.

The Diversity Outbred (DO) is a highly engineered mouse population derived from eight genetically diverse inbred founders (A/J, C57BL/6J, 129S1/SvImJ, NOD/ShiLtJ, NZO/HILtJ, CAST/EiJ, PWK/PhJ, and WSB/EiJ) [16]. The DO has been randomly mated for over 30 generations and, as a result, it enables high-resolution genetic mapping and relatively efficient identification of causal genes [17,18]. As an outbred stock, the DO also more closely approximates the highly heterozygous genomes of a human population. These attributes, coupled with the ability to perform detailed and in-depth characterization of bone traits and generate molecular data on bone, position the DO as a platform to assist in addressing the limitations of human studies described above.

Here, we created a resource for the systems genetics of bone strength consisting of information on 55 bone traits from over 600 DO mice, and RNA-seq data from marrow-depleted cortical bone in 192 DO mice. We demonstrated the utility of this resource in two ways. First, we applied a network approach to the bone transcriptomics data in the DO and identified 72 genes that were bone-associated nodes in Bayesian networks, and their human homologs were located in BMD GWAS loci and regulated by colocalizing eQTL in human tissues. Of the 72, 21 were not previously known to

influence bone. The further investigation of two of the 21 novel genes, *SERTAD4* and *GLT8D2*, revealed that they were likely causal and influenced BMD via a role in osteoblasts. Second, we performed GWASs in the DO for 55 complex traits associated with bone strength; identifying 28 QTL. By integrating QTL and bone eQTL data in the DO, we identified *Qsox1* as the gene responsible for a QTL on Chromosome (Chr.) 1 influencing cortical bone accrual along the medial-lateral femoral axis and femoral strength. These data highlight the power of the DO mouse resource to complement and inform human genetic studies of osteoporosis.

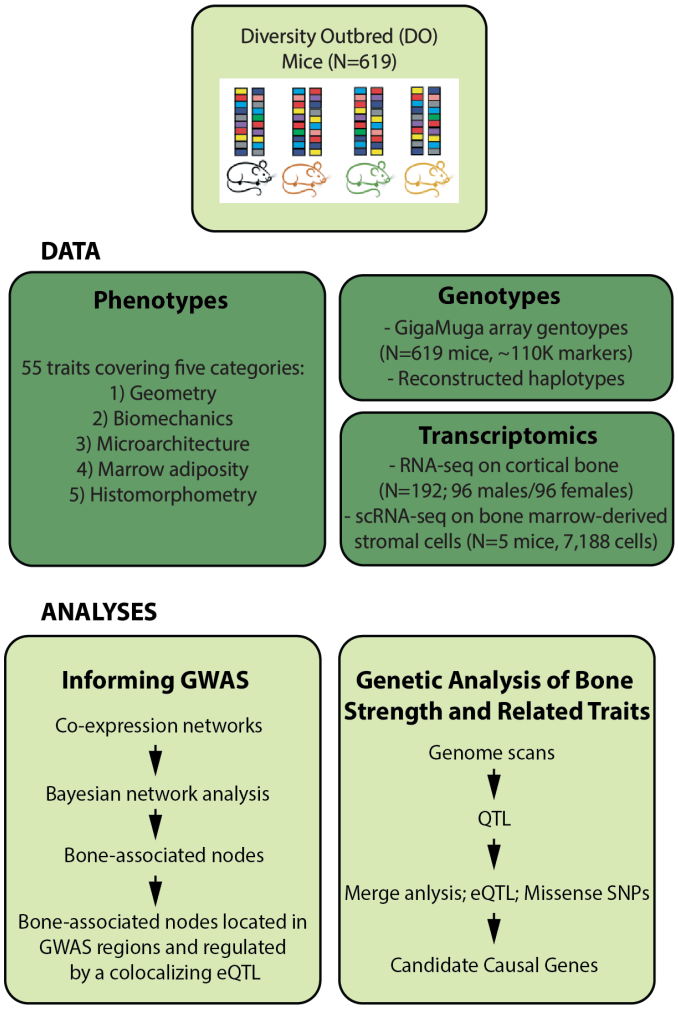

Figure 1. Resource overview. An overview of the resource including data generated and analyses performed.

RESULTS:

Development of a resource for the systems genetics of bone strength:

An overview of the resource is presented in **Figure 1**. We measured 55 complex skeletal phenotypes in a cohort of DO mice (N=619; 314 males, 305 females; breeding generations 23-33) at 12 weeks of age. We also generated RNA-seq data from marrow-depleted femoral diaphyseal bone from a randomly chosen subset of

the 619 phenotyped mice (N=192; 96/sex). All 619 mice were genotyped using the GigaMUGA[19] array (~110K SNPs) and these data were used to reconstruct the genome-wide haplotype structures of each mouse. As expected, the genomes of DO mice consisted of approximately 12.5% from each of the eight

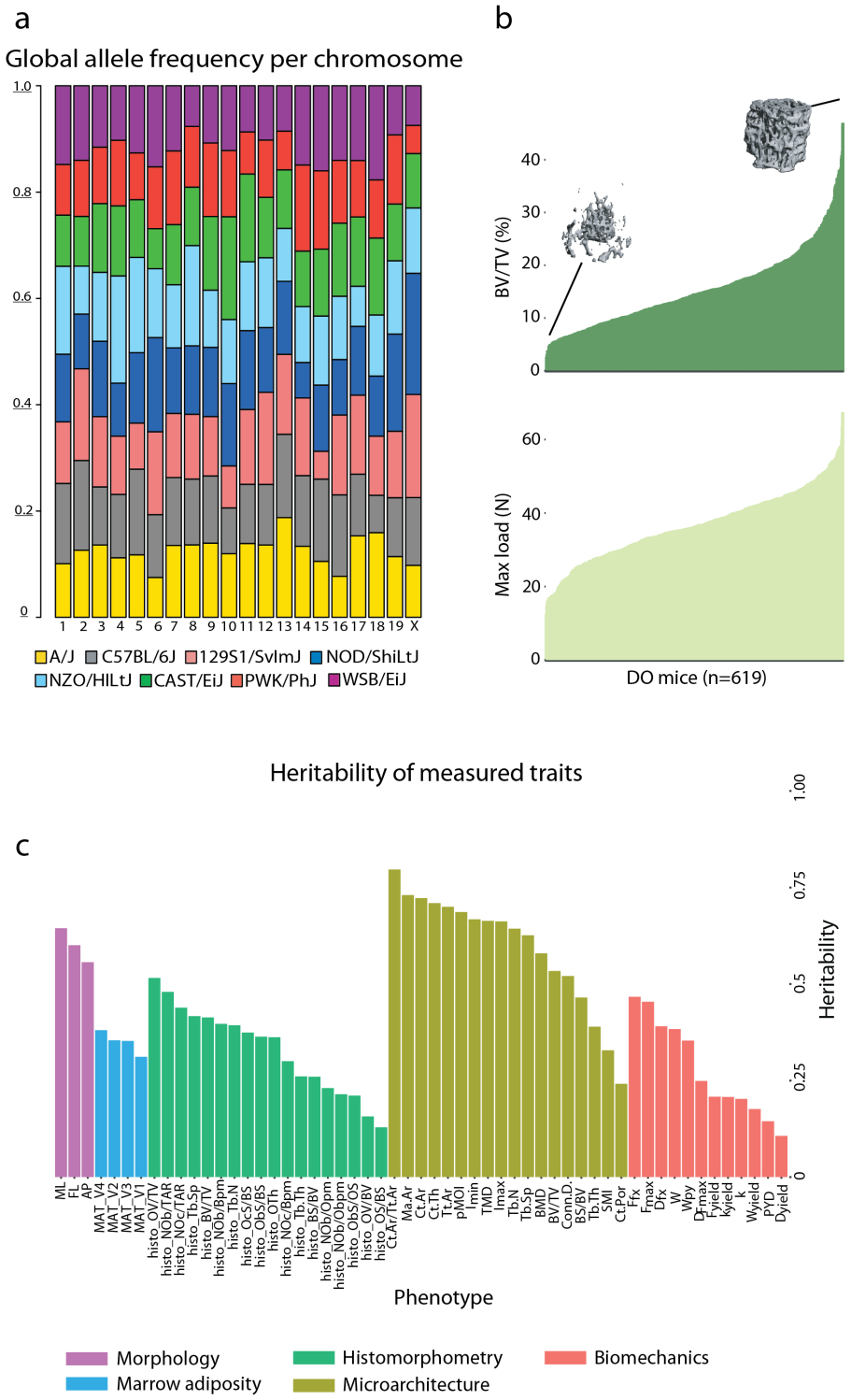

Figure 2. Characterization of the experimental cohort. a) Allele frequency per chromosome, across the DO mouse cohort. **b**) Bone volume fraction and max load across the DO cohort. Insets are microCT images representing low and high bone volume fraction. **c**) Heritability of each trait. Phenotypes are colored by phenotypic category.

143 DO founders (**Figure 2A**).

144

145 The collection of phenotypes included measures of bone morphology,
146 microarchitecture, and biomechanics of the femur, along with tibial histomorphometry
147 and marrow adiposity (**Supplemental Tables 1 and 2)**. Our data included quantification
148 of femoral strength as well as many clinically relevant predictors of strength and fracture
149 risk (*e.g.*, trabecular and cortical microarchitecture). Traits in all categories (except tibial
150 marrow adipose tissue (MAT)) were significantly (P_{adj}<0.05) correlated with femoral
151 strength (**Supplemental Table 3**). Additionally, all traits exhibited substantial variation
152 across the DO cohort. For example, we observed a 30.8-fold variation (the highest
153 measurement was 30.8 times greater than the lowest measurement) in trabecular bone
154 volume fraction (BV/TV) of the distal femur and 5.6-fold variation in femoral strength
155 (**Figure 2B)**. After adjusting for covariates (age, DO generation, sex, and body weight)
156 all traits had non-zero heritabilities (h^2) (**Figure 2C**). Correlations between traits in the
157 DO were consistent with expected relationships observed in previous mouse and
158 human studies (**Supplemental Table 4)** [20–23].

159

160 In addition to standard RNA-seq quality control procedures (**Methods**), we also
161 assessed RNA-seq quality by principal components analysis (PCA) and as expected,
162 we identified effects of sex (PC3) and batch (**Supplemental Figure 1**), which we then
163 corrected for prior to downstream analyses. Importantly, our PCA analysis did not
164 identify any outliers in the bulk RNA-seq data Furthermore, we performed differential
165 expression analyses between sexes and between individuals with high versus low bone

strength (**Supplemental Tables 5 and 6**). As expected, the most significantly differentially expressed genes based on sex were located on the X chromosome. We identified 83 significantly (FDR<0.05) differentially-expressed transcripts in the analysis of low and high bone strength. Many were genes, such as *Ahsg* [24] and *Arg1* [25], which have previously been implicated in the regulation of bone traits.

Identification of bone-associated nodes:

We wanted to address the challenge of identifying causal genes from BMD GWAS data, using the DO resource described above. To do so, we employed a network-based approach

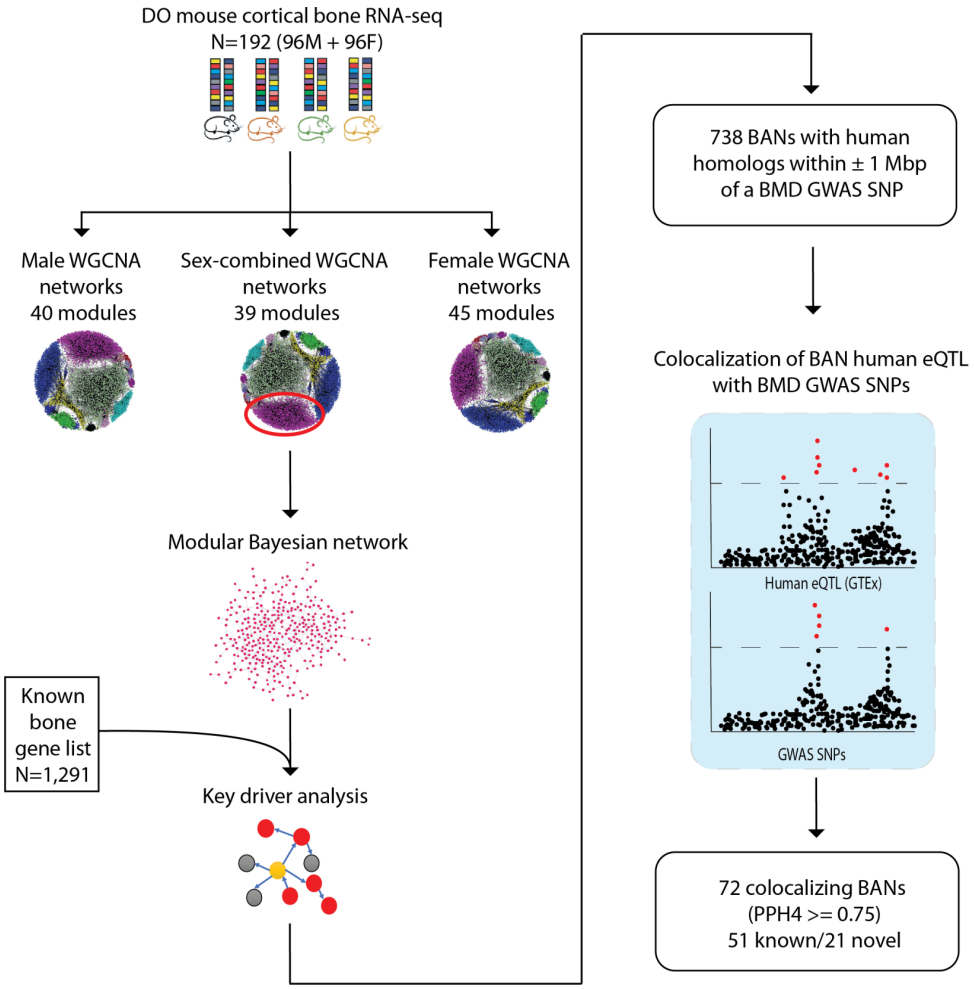

Figure 3. Overview of the network approach used to identify genes potentially responsible for BMD GWAS loci. Three WGCNA networks (124 total modules) were constructed from RNA-seq data on cortical bone in the DO (N=192). A Bayesian network was then learned for each module. We performed key driver analysis on each Bayesian network to identify bone-associated nodes (BANs), by identifying nodes (genes) that were more connected to more known bone genes than was expected by chance. We colocalized GTEx human eQTL for each BAN with GWAS BMD SNPs to identify potentially causal genes at BMD GWAS loci.

189 similar to one we have used in prior studies [26,27] (**Figure 3**). First, we partitioned genes
190 into groups based on co-expression by applying weighted gene co-expression network
191 analysis (WGCNA) to the DO cortical bone RNA-seq data [28]. We generated three
192 WGCNA networks; sex-combined, male, and female. The three networks contained a
193 total of 124 modules (**Supplemental Table 7**)**.** A Gene Ontology (GO) analysis revealed
194 that nearly all modules were enriched for genes involved in specific biological
195 processes, including modules enriched for processes specific to bone cells (osteoblasts
196 or osteoclasts) (**Supplemental Table 8**).
197
198 We next sought to infer causal interactions between genes in each module, and then
199 use this information to identify genes likely involved in regulatory processes relevant to
200 bone and the regulation of BMD. To do so, we generated Bayesian networks for each
201 co-expression module, allowing us to model directed gene-gene relationships based on
202 conditional independence. Bayesian networks allowed us to model causal links between
203 co-expressed (and likely co-regulated) genes.
204

205 We hypothesized that key genes involved in bone regulatory processes would play
206 central roles in bone networks and, thus, be more highly connected in the Bayesian
207 networks. In order to test this hypothesis, we generated a list of genes implicated in
208 processes known to impact bone or bone cells ("known bone gene" list (N=1,291);
209 **Supplemental Table 9**; see **Methods)**. The GWAS loci referenced in this study were
210 enriched in human homologs of genes in the "known bone list", relative to the set of
211 protein-coding genes in the genome (OR=1.35, $P=1.45^{-7}$). Across the three network

212 sets (combined, male and female), we found that genes with putative roles in bone
213 regulatory processes were more highly connected than all other genes ($P=2.6 \times 10^{-5}$,
214 $P=5.2 \times 10^{-3}$, and $P=5.5 \times 10^{-7}$ for combined, male, and female network sets,
215 respectively), indicating the structure of the Bayesian networks was not random with
216 respect to connectivity.

217

218 To discover genes potentially responsible for GWAS associations, we identified bone-
219 associated nodes (BANs). BANs were defined as genes connected in our Bayesian
220 networks with more genes in the "known bone gene" list than would be expected by
221 chance [29–32]. The analysis identified 1,465 genes with evidence ($P_{nominal}<0.05$) of being a
222 BAN (*i.e.,* sharing network connections with genes known to participate in a bone
223 "regulatory" process) (**Supplemental Table 10**).

224

225 **Using BANs to inform human BMD GWAS:**

226 We reasoned that the BAN list was enriched for causal BMD GWAS genes. In fact, of
227 the 1,465 BANs, 1,251 had human homologs and 738 of those were within 1 Mbp of
228 one of the 1,161 BMD GWAS lead SNPs identified in [3] and [5]. This represents an
229 enrichment of BANs within GWAS loci (+/- 1Mbp of GWAS SNP), relative to the number
230 of protein-coding genes within GWAS loci (OR=1.28, $P=1.97 \times 10^{-5}$).

231

232 However, a gene being a BAN is likely not strong evidence, by itself, that a particular
233 gene is causal for a BMD GWAS association. Therefore, to provide additional evidence
234 connecting BMD-associated variants to the regulation of BANs, we identified local eQTL

235 for each BAN homolog in 48 human non-bone samples using the Gene Tissue
236 Expression (GTEx) project [10,33,34]. Our rationale for using GTEx was that while these
237 data do not include information on bone tissues or bone cells, a high degree of local
238 eQTL sharing has been observed between GTEx tissues [10,35]. This suggests that a
239 colocalizing eQTL in a non-bone tissue may represent either a non-bone autonomous
240 causal effect or may reflect the actions of a shared eQTL that is active in bone and
241 shared across non-bone tissues. We then tested each eQTL for colocalization (*i.e.*,
242 probability the eQTL and GWAS association share a common causal variant) with their
243 respective BMD GWAS association [3,5]. Of the 738 BANs located in proximity of a BMD
244 GWAS locus, 72 had colocalizing eQTL (PPH4≥0.75, **Supplemental Table 11,** see
245 **Methods**) in at least one GTEx tissue (**Table 1**). Of these, 51 (70.8%) were putative
246 regulators of bone traits (based on comparing to the known bone gene list (N=40) and a
247 literature search for genes influencing bone cell function (N=11)), highlighting the ability
248 of the approach to recover known biology. Based on overlap with the known bone gene
249 list, this represents a highly significant enrichment of known bone genes in the list of
250 BANs with colocalizing eQTL relative to the number of known bone genes in the list of
251 GWAS-proximal BANs (OR=2.53, P=1.65 x 10^{-4}). Our approach identified genes such
252 as *SP7* (Osterix) [36], *SOST* [37,38], and *LRP5* [39–41], which play central roles in osteoblast-
253 mediated bone formation. Genes essential to osteoclast activity, such as *TNFSF11*
254 (RANKL) [42–45], *TNFRSF11A* (RANK) [46,47], and *SLC4A2* [48] were also identified. Twenty-
255 one (29.2%) genes were not previously implicated in the regulation of bone traits**.**
256

257 One of the advantages of the network approach is the ability to identify potentially
258 causal genes and provide insight into how they may impact BMD based on their module
259 membership and network connections. For example, the "cyan" module in the female
260 network (cyan_F) harbored many of the known BANs that influence BMD through a role
261 in osteoclasts (the GO term "osteoclast differentiation" was highly enriched $P=2.8 \times 10^{-}$
262 ^{15} in the cyan_F module) (**Supplemental Table 8**). Three of the twenty-one novel BANs
263 with colocalizing eQTL (**Table 1**), *ATP6V1A*, *PRKCH* and *AMZ1*, were members of the
264 cyan module in the female network. Based on their cyan module membership it is likely
265 they play a role in osteoclasts. *ATP6V1A* is a subunit of the vacuolar ATPase V1
266 domain [49]. The vacuolar ATPase plays a central role in the ability of osteoclasts to
267 acidify matrix and resorb bone, though *ATP6V1A* itself (which encodes an individual
268 subunit) has not been directly connected to the regulation of BMD [49]. *PRKCH* encodes
269 the eta isoform of protein kinase C and is highly expressed in osteoclasts [50]. *AMZ1* is a
270 zinc metalloprotease and is relatively highly expressed in osteoclasts, and is highly
271 expressed in macrophages, which are osteoclast precursors [50].
272
273 **Table 1. Homologous human BANs with colocalizing eQTL. Genes in bold are known**
274 **bone genes.**

Gene	WGCNA module	PPH4	# neighbors	# bone neighbors	BAN P-value	Tissue of strongest colocalizing eQTL
ADAM12	Brown_F	0.90	13	5	4.0×10^{-3}	Testis
AMZ1	Cyan_F	0.87	18	4	4.3×10^{-2}	Thyroid
ADGRD1	Yellow_M	0.93	9	4	6.5×10^{-3}	Testis
ARHGAP1	Blue_M	0.99	8	3	3.2×10^{-2}	Muscle_Skeletal
ATP2B2	Pink_F	0.79	10	3	3.5×10^{-2}	Lung

ATP6V1A	Cyan_C	0.87	33	12	$1.5x10^{-5}$	Nerve_Tibial
B4GALNT3	Brown_F	0.99	7	3	$1.9x10^{-2}$	Artery_Coronary
BICC1	Brown_C	0.76	16	4	$4.8x10^{-2}$	Brain_Caudate_basal_ganglia
BMP8A	Yellow_M	0.82	12	5	$3.2x10^{-3}$	Nerve_Tibial
CAVIN1	Pink_F	0.76	4	2	$4.3x10^{-2}$	Esophagus_Muscularis
CCR1	Cyan_C	0.99	50	11	$4.0x10^{-3}$	Whole_Blood
CD109	Brown_C	0.86	22	6	$1.1x10^{-2}$	Spleen
CKB	Cyan_C	0.96	18	9	$8.0x10^{-6}$	Artery_Aorta
COPZ2	Brown_C	0.91	11	3	$4.4x10^{-2}$	Testis
COX4I2	Red_F	0.98	11	3	$4.5x10^{-2}$	Muscle_Skeletal
DOCK9	Red_F	0.98	9	5	$5.5x10^{-4}$	Nerve_Tibial
EN2	Blue_C	0.84	31	6	$2.5x10^{-2}$	Colon_Sigmoid
FAM3C	Brown_C	0.84	30	6	$4.6x10^{-2}$	Heart_Left_Ventricle
FAT1	Yellow_M	0.97	8	3	$3.2x10^{-2}$	Heart_Left_Ventricle
FGFRL1	Turquoise_F	0.99	11	4	$1.3x10^{-2}$	Muscle_Skeletal
FRZB	Brown_F	0.99	7	3	$1.9x10^{-2}$	Nerve_Tibial
GBA	Cyan_F	0.94	17	5	$1.5x10^{-2}$	Nerve_Tibial
GHR	Turquoise_F	0.95	11	3	$4.5x10^{-2}$	Lung
GJA1	Brown_C	0.89	11	4	$1.2x10^{-2}$	Nerve_Tibial
GLT8D2	Royalblue_M	0.88	21	5	$4.1x10^{-2}$	Pituitary
GNA12	Darkturquoise_C	0.91	40	7	$2.7x10^{-2}$	Lung
GREM2	Greenyellow_F	0.99	10	4	$8.9x10^{-3}$	Artery_Tibial
IBSP	Brown_C	0.99	48	8	$2.5x10^{-2}$	Muscle_Skeletal
IGDCC4	Brown_C	0.87	52	8	$3.8x10^{-2}$	Adrenal_Gland
IHH	Red_C	0.89	7	3	$1.9x10^{-2}$	Esophagus_Gastroesophageal_Junction
ITPKB	Green_M	0.84	11	3	$4.9x10^{-2}$	Colon_Sigmoid
KDELR3	Brown_C	0.78	17	4	$3.4x10^{-2}$	Testis

KLC1	Turquoise_C	0.81	26	5	$4.1x10^{-2}$	Esophagus_Gastroesophageal_Junction
LRP4	Brown_C	0.96	13	4	$2.3x10^{-2}$	Pancreas
LRP5	Yellow_M	0.92	5	3	$7.1x10^{-3}$	Pancreas
MDK	Brown_C	0.97	9	3	$4.0x10^{-2}$	Colon_Sigmoid
MEPE	Red_F	0.8	20	7	$1.3x10^{-3}$	Lung
MMP14	Brown_C	0.83	27	10	$6.3x10^{-5}$	Adrenal_Gland
MPRIP	Yellow_M	0.75	15	5	$9.6x10^{-3}$	Adipose_Subcutaneous
MRC2	Brown_F	0.99	3	2	$2.3x10^{-2}$	Adipose_Subcutaneous
MYPOP	Turquoise_C	0.78	7	3	$1.9x10^{-2}$	Esophagus_Muscularis
NAB2	Brown_F	0.77	32	6	$3.1x10^{-2}$	Skin_Sun_Exposed_Lower_Leg
NEK6	Yellow_M	0.97	4	2	$4.6x10^{-2}$	Thyroid
NPR2	Turquoise_M	0.86	8	3	$3.2x10^{-2}$	Liver
PAPSS2	Green_M	0.91	10	3	$3.8x10^{-2}$	Testis
PGF	Brown_C	0.75	11	3	$4.4x10^{-2}$	Colon_Sigmoid
PJA2	Turquoise_F	0.96	11	3	$4.5x10^{-2}$	Thyroid
PKD1	Midnightblue_M	0.88	13	4	$2.7x10^{-2}$	Nerve_Tibial
PKDCC	Turquoise_C	0.93	15	4	$3.9x10^{-2}$	Brain_Cerebellum
PLEKHM1	Cyan_C	0.78	18	5	$1.8x10^{-2}$	Brain_Cerebellum
PLS1	Black_M	0.87	17	4	$3.9x10^{-2}$	Artery_Aorta
PRKCH	Cyan_C	0.78	33	9	$1.9x10^{-3}$	Muscle_Skeletal
PSTPIP1	Yellow_C	0.88	41	8	$2.6x10^{-2}$	Nerve_Tibial
RASD1	Tan_C	0.88	38	8	$1.7x10^{-2}$	Stomach
SBNO2	Brown_M	0.99	25	5	$4.2x10^{-2}$	Esophagus_Mucosa
SERTAD4	Royalblue_M	0.77	13	6	$6.4x10^{-4}$	Adipose_Subcutaneous
SH3RF3	Greenyellow_F	0.99	15	4	$4.0x10^{-2}$	Cells_Transformed_fibroblasts
SLC4A2	Cyan_F	0.99	19	7	$9.2x10^{-4}$	Testis

SLC7A7	Green_M	0.86	3	2	$2.5x10^{-2}$	Prostate
SMAD9	Red_C	0.92	22	7	$2.3x10^{-3}$	Colon_Transverse
SOCS2	Brown_F	0.96	6	3	$1.2x10^{-2}$	Cells_Transformed_fibroblasts
SOST	Red_C	0.95	24	8	$7.8x10^{-4}$	Brain_Frontal_Cortex_BA9
SP7	Brown_C	0.96	13	4	$2.3x10^{-2}$	Testis
SPP1	Cyan_C	0.99	29	7	$1.2x10^{-2}$	Nerve_Tibial
THBS3	Darkorange_C	0.98	22	5	$4.1x10^{-2}$	Colon_Sigmoid
TNFRSF11A	Cyan_F	0.79	14	8	$7.9x10^{-6}$	Whole_Blood
TNFRSF11B	Red_C	0.93	47	8	$2.2x10^{-2}$	Heart_Atrial_Appendage
TNFSF11	Lightcyan_F	0.76	9	4	$5.8x10^{-3}$	Cells_EBV-transformed_lymphocytes
UBE2R2	Red_M	0.93	15	4	$4.5x10^{-2}$	Cells_Transformed_fibroblasts
ZC2HC1C	Turquoise_C	0.96	19	4	$4.9x10^{-2}$	Adipose_Subcutaneous
ZFYVE21	Red_M	0.92	16	4	$3.2x10^{-2}$	Breast_Mammary_Tissue
ZNF609	Turquoise_C	0.78	9	3	$3.9x10^{-2}$	Whole_Blood

Next, we focused on two of the novel BANs with colocalizing eQTL, *SERTAD4* (GTEx Adipose Subcutaneous; coloc PPH4=0.77; PPH4/PPH3=7.9) and *GLT8D2* (GTEx Pituitary; coloc PPH4=0.88; PPH4/PPH3=13.4). Both genes were members of the royalblue module in the male network (royalblue_M). The function of *SERTAD4* (SERTA domain-containing protein 4) is unclear, though proteins with SERTA domains have been linked to cell cycle progression and chromatin remodeling [51]. *GLT8D2* (glycosyltransferase 8 domain containing 2) is a glycosyltransferase linked to nonalcoholic fatty liver disease [52]. In the DO, the eigengene of the royalblue_M module was significantly correlated with several traits, including trabecular number (Tb.N; rho=-

285 0.26; P=9.5 x 10^{-3}) and separation (Tb.Sp; rho=0.27; P=7.1 x 10^{-3}), among others
286 (**Supplemental Table 12**). The royalblue_M module was enriched for genes involved in
287 processes relevant to osteoblasts such as “extracellular matrix” (P=8.4 x 10^{-19}),
288 “endochondral bone growth” (P=5.7 x 10^{-4}), “ossification” (P=8.9 x 10^{-4}) and “negative
289 regulation of osteoblast differentiation” (P=0.04) (**Supplemental Table 8**). Additionally,
290 *Sertad4* and *Glt8d2* were connected, in their local (3-step) Bayesian networks, to well-
291 known regulators of osteoblast/osteocyte biology (such as *Wnt16* [53], *Postn* [54,55], and
292 *Col12a1* [56] for *Sertad4* and *Pappa2* [57], *Pax1* [57,58], and *Tnn* [59] for *Glt8d2*) (**Figure 4A and**
293 **4B**). *Sertad4* and *Glt8d2* were strongly expressed in calvarial osteoblasts with
294 expression increasing (P<2.2 x 10^{-16} and P=6.4 x 10^{-10}, respectively) throughout the
295 course of differentiation (**Figure 4C**). To further investigate their expression in
296 osteoblasts, we generated single-cell RNA-seq (scRNA-seq) data on mouse bone
297 marrow-derived stromal cells exposed to osteogenic differentiation media *in vitro* from
298 our mouse cohort (N=5 mice (4 females, 1 male), 7,188 cells, **Supplemental Table 13**,
299 **Supplemental Figure 2**). Clusters of cell-types were grouped into mesenchymal
300 progenitors, preadipocytes/adipocytes, osteoblasts, osteocytes, and non-osteogenic
301 cells based on the expression of genes defining each cell-type (**Supplemental Table**
302 **14**). *Sertad4* was expressed across multiple cell-types, with its highest expression in a
303 specific cluster (cluster 9) of mesenchymal progenitor cells and lower levels of
304 expression in osteocytes (cluster 10) (**Figure 4D, Supplemental Figure 3**). *Glt8d2* was
305 expressed in a relatively small number of cells in both progenitor and mature osteoblast
306 populations (**Figure 4D, Supplemental Figure 3**).
307

308 Finally, we analyzed data from the International Mouse Phenotyping Consortium (IMPC)
309 for *Glt8d2* [60]. After controlling for body weight, there was a significant (P=1.5 x 10^{-3})
310 increase in BMD in male *Glt8d2*$^{-/-}$ and no effect (P=0.88) in female *Glt8d2*$^{-/-}$ mice (sex
311 interaction P= 6.9 x 10^{-3}) **(Figure 4E)**. These data were consistent with the direction of
312 effect predicted by the human *GLT8D2* eQTL and eBMD GWAS locus where the effect
313 allele of the lead eBMD SNP (rs2722176) was associated with increased *GLT8D2*
314 expression and decreased BMD. Together, these data suggest that *SERTAD4* and
315 *GLT8D2* are causal for their respective BMD GWAS associations and they likely impact
316 BMD through a role in modulating osteoblast-centric processes.
317
318 **Identification of QTLs for strength-related traits in the DO:**

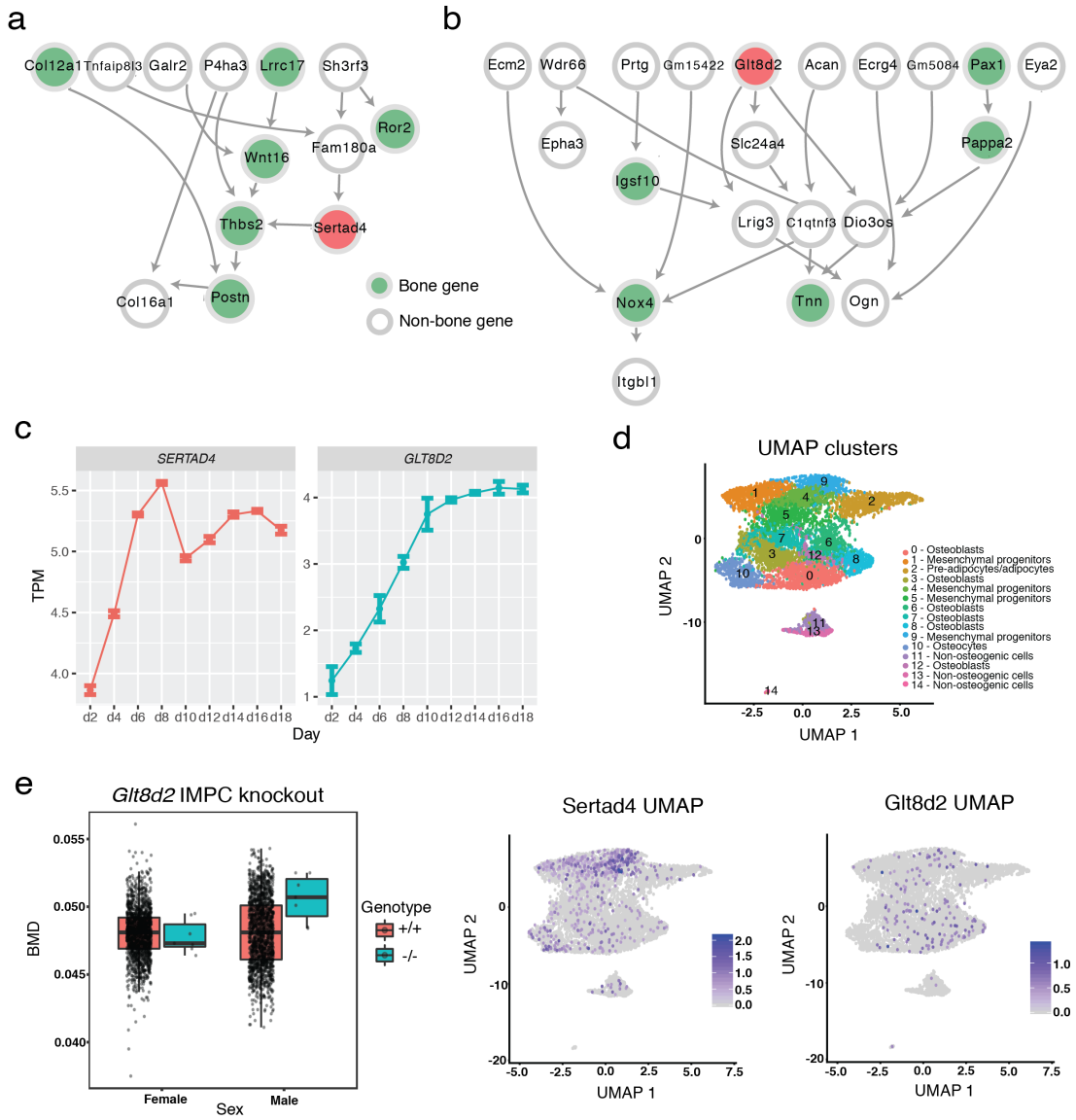

Figure 4. Identifying *SERTAD4* and *GLT8D2* as putative regulators of BMD. a) Local 3-step neighborhood around *Sertad4*. Known bone genes highlighted in green. *Sertad4* highlighted in red. **b**) Local 3-step neighborhood around *Glt8d2*. Known bone genes highlighted in green. *Glt8d2* highlighted in red. **c**) Expression of *Sertad4* and *Glt8d2* in calvarial osteoblasts. Error bars represent the standard error of the mean. **d**) Single cell RNA-seq expression data. Each point represents a cell. The top panel shows UMAP clusters and their corresponding cell-type. The bottom two panels show the expression of *Sertad4* and *Glt8d2.* **e**) Bone mineral density in *Glt8d2* knockout mice from the IMPC. The center line is the median, and the whiskers represent 1.5 x IQR.

The other key limitation of human genetic studies of osteoporosis has been the strict focus on BMD, though many other aspects of bone influence its strength. To directly

322 address this limitation using the DO, we performed GWAS for 55 complex skeletal traits.
323 This analysis identified 28 genome-wide significant (permutation-derived P<0.05) QTLs
324 for 20 traits mapping to 10 different loci (defined as QTL with peaks within a 1.5 Mbp
325 interval) (**Table 2 and Supplemental Figure 4**). These data are presented interactively
326 in a web-based tool (http://qtlviewer.uvadcos.io/). Of the 10 loci, four impacted a single
327 trait (*e.g.,* medial-lateral femoral width (ML) QTL on Chr2@145.4Mbp), while the other
328 six impacted more than one trait (*e.g.*, cortical bone morphology traits, cortical tissue
329 mineral density (TMD), and cortical porosity (Ct.Por) QTL on Chr1@155Mbp). The 95%
330 confidence intervals (CIs) for the 21 autosomal associations ranged from 615 Kbp to 5.4
331 Mbp with a median of 1.4 Mbp.
332
333 **Table 2. QTL identified for complex skeletal traits in the DO**

Locus	Trait	LOD	Chr.	Position (Mbp)	95% CI (Mbp)	# missense variants	Genes with colocalizing eQTL
1	TMD	23.9	1	155.1	154.8 - 155.6	7	*Ier5*
1	Ma.Ar	12.8	1	155.3	155.1 - 155.7	7	*Ier5, Qsox1*
1	Tt.Ar	11.5	1	155.2	155.1 - 156.2	7	*Ier5, Qsox1*
1	Ct.Por	11.4	1	155.4	155.1 - 156.4	7	*Ier5, Qsox1*
1	ML	10	1	155.4	155.1 - 155.7	7	*Ier5, Qsox1*
1	pMOI	8.8	1	155.1	154.8 - 158.2	7	*Ier5, Qsox1*
1	Ct.Ar/Tt.Ar	8.5	1	155.3	154.3 - 155.7	7	*Ier5, Qsox1*
1	Imax	8.3	1	155.1	155.1 - 158.2	7	*Ier5, Qsox1*
2	ML	7.9	2	145.4	144.1 - 145.6	-	-
3	Ma.Ar	8.8	3	68.1	66.6 - 70	8	*Mfsd1, Il12a, Gm17641, 1110032F04Rik*
4	Ma.Ar	8	4	114.6	113 - 118.4	-	-
4	Tt.Ar	8.2	4	114.6	113.6 - 114.8	-	-
5	Ct.Ar/Tt.Ar	8.1	4	127.7	125.4 - 128.1	-	*Csf3r, Gm12946, Clspn, Ncdn, Gm12941, Zmym6, Gm25600*
6	BMD	7.8	8	103.5	102.7 - 104.4	-	-

7	TMD	14.6	10	23.5	23.1 - 24.6	-	-
7	W	13.6	10	24.3	23.5 - 24.6	-	-
7	Wpy	11.9	10	23.8	23.5 - 25.3	-	-
7	Dfx	10.7	10	23.7	23.3 - 24.6	-	-
7	DFmax	9.4	10	23.7	21.8 - 25.2	-	*C920009B18Rik*
8	Fmax	8.8	16	23.3	22.3 - 23.4	-	-
8	Ffx	8.2	16	23.1	22.6 - 23.4	-	-
9	Ct.Ar	13.5	X	59.4	58.4 - 71.2	-	-
9	Imax	11	X	59.5	58.4 - 69.6	-	-
9	pMOI	10.4	X	59.4	58.4 - 61.4	-	-
9	Imin	8.4	X	59.5	57.3 - 61.2	-	*Zic3*
10	Ct.Th	9.9	X	73.4	58.4 - 74.1	-	-
10	TbSp	8.6	X	73.8	72.7 - 77.5	-	*Pls3*
10	Tb.N	7.9	X	74	72.7 - 76.8	-	*Fundc2, Cmc4, Pls3*

Overlap with human BMD GWAS:

We anticipated the genetic analysis of bone strength traits in DO mice would uncover novel biology not captured by human BMD GWAS. To evaluate this prediction, we identified overlaps between the 10 identified mouse loci and human BMD GWAS associations [3,5]. Of the 10 mouse loci, the human syntenic regions (**Supplemental Table 15**) for six (60%) contained at least one independent GWAS association (**Supplemental Figure 5**). We calculated the number expected by chance by randomly selecting 10 human regions (of the same size) 1000 times, followed by identifying overlaps. Six overlaps corresponded to the 57th percentile of the null distribution.

Identification of potentially causal genes:

For each locus, we defined the causal gene search space as the widest confidence interval given all QTL start and end positions ±250 Kbp. We then used a previously described approach, merge analysis, to fine-map QTL and identify likely causal genes

(**Figure 5**) [61]. Merge analysis was performed by imputing all known variants from the genome sequences of the eight founders onto haplotype reconstructions for each DO mouse, and then performing single variant association tests. We focused on variants in the top 15% of each merge analysis as those are most likely to be causal [61].

We next identified missense variants that were top merge analysis variants common to all QTL in a locus. We identified seven missense variants in

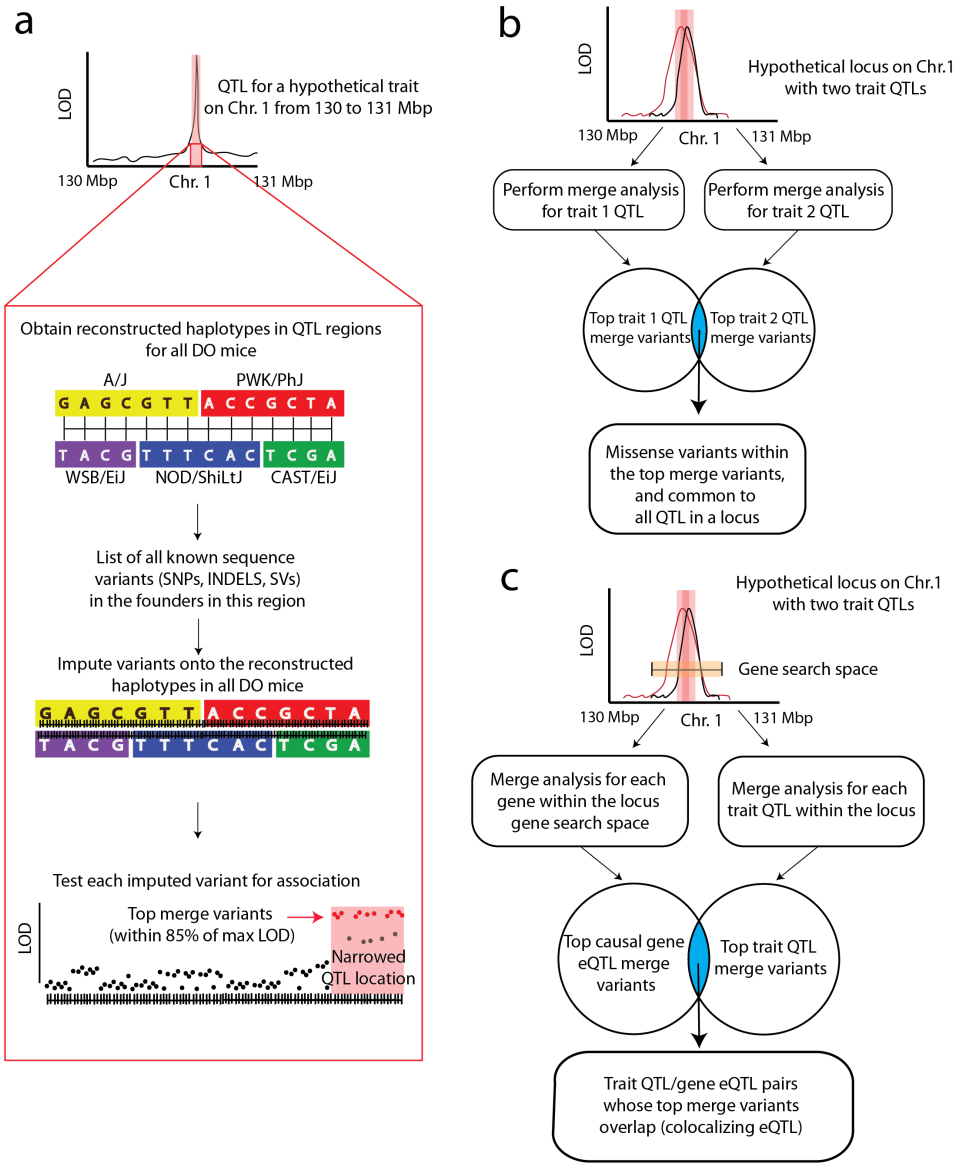

Figure 5. Overview of our approach to QTL fine-mapping. a) Overview of merge analysis. **b**) Overview of merge analysis as performed for the identification of missense variants. **c**) Overview of merge analysis as performed for the identification of colocalizing trait QTL/ gene eQTL within a locus. The pink columns around the QTL in each association plot represent the QTL 95% confidence intervals. The yellow box in panel (**c**) represents the gene search space for a locus, defined as the region within ± 250 Kbp around the outer boundaries of the 95% confidence intervals within a locus.

373 locus 1, and eight missense variants in locus 3 (**Table 2**). Of the seven missense
374 variants in locus 1, three (rs243472661, rs253446415, and rs33686629) were predicted
375 to be deleterious by SIFT. They are all variants in the uncharacterized protein coding
376 gene *BC034090*. In locus 3, three (rs250291032, rs215406048 and rs30914256) were
377 predicted to be deleterious by SIFT (**Supplemental Table 16**). These variants were
378 located in myeloid leukemia factor 1 (*Mlf1*), Iqcj and Schip1 fusion protein (*Iqschfp*), and
379 Retinoic acid receptor responder 1 (*Rarres1*), respectively.
380
381 We next used the cortical bone RNA-seq data to map 10,399 local eQTL in our DO
382 mouse cohort (**Supplemental Table 17**). Of these, 174 local eQTL regulated genes
383 located within bone trait QTL. To identify colocalizing eQTL, we identified trait
384 QTL/eQTL pairs whose top merge analysis variants overlapped. This analysis identified
385 18 genes with colocalizing eQTL in 6 QTL loci (**Table 2**).
386
387 **Characterization of a QTL on Chromosome 1 influencing bone morphology:**
388 Locus 1 (Chr1) influenced cortical bone morphology (Ma.Ar, total cross sectional area
389 (Tt.Ar), medial-lateral femoral width (ML), polar moment of inertia (pMOI), cortical bone
390 area fraction (Ct.Ar/Tt.Ar), and maximum moment of inertia (I_{max})), tissue mineral
391 density (TMD), and cortical porosity (Ct.Por) (**Figure 6A**). We focused on this locus due
392 to its strong effect size and the identification of candidate genes (*Ier5*, *Qsox1,* and
393 *BC034090*) (**Table 2**). Additionally, we had previously measured ML in an independent
394 cohort of DO mice (N=577; 154 males/423 females) from earlier generations
395 (generations G10 and G11) and a QTL scan of those data uncovered the presence of a

396 similar QTL on Chr1 [62] (**Supplemental Figure 6, Methods**). The identification of this

397 locus across two different DO cohorts (which differed in generations, diets, and ages)

398 provided robust replication justifying further analysis.

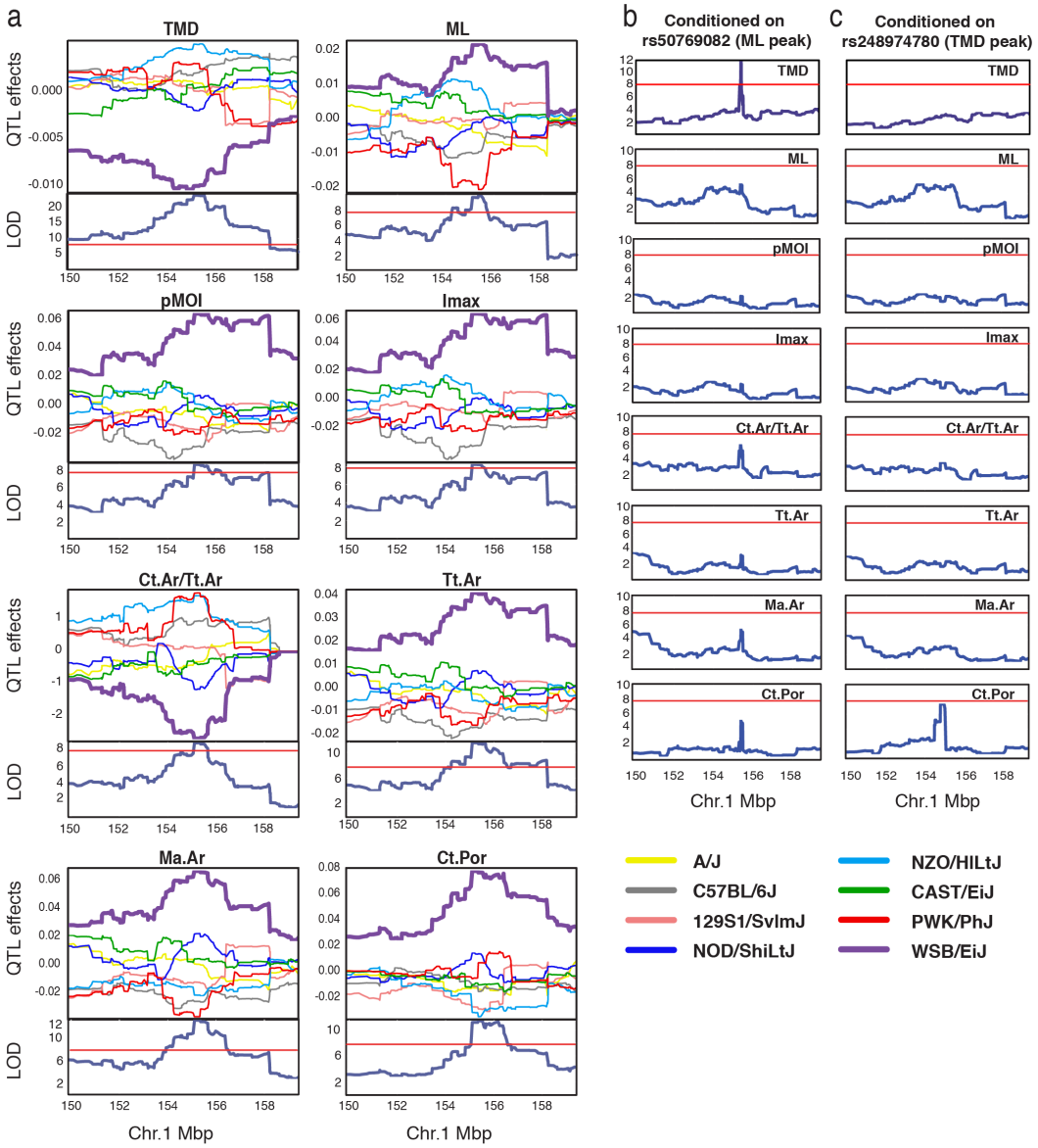

Figure 6. QTL (locus 1) on chromosome 1. a) For each plot, the top panel shows allele effects for the DO founders for each of the 8 QTL across an interval on chromosome 1 (Mbp, colors correspond to the founder allele in the legend). Bottom panels show each respective QTL scan. The red horizontal lines represent LOD score thresholds (Genome-wide P<=0.05). **b**) QTL scans across the same interval as panel (A), after conditioning on rs50769082. **c**) QTL scans after conditioning on rs248974780.

399

400 The traits mapping to this locus fell into two phenotypic groups, those influencing
401 different aspects of cross-sectional size (e.g., ML and Tt.Ar) and TMD/cortical porosity.
402 We suspected that locus 1 QTL underlying these two groups were distinct, and that QTL
403 for traits within the same phenotypic group were linked. This hypothesis was further
404 supported the observation that correlations among the size traits were strong and cross-
405 sectional size traits were not correlated with TMD or porosity **(Supplemental Table 4)**.
406 Therefore, we next tested if the locus affected all traits or was due to multiple linked
407 QTL. The non-reference alleles of the top merge analysis variants for each QTL were
408 private to WSB/EiJ. To test if these variants explained all QTL, we performed the same
409 association scans for each trait, but included the genotype of the lead ML QTL variant
410 (rs50769082; 155.46 Mbp; ML was used as a proxy for all the cortical morphology traits)
411 as an additive covariate. This led to the ablation of all QTL except for TMD which
412 remained significant (**Figure 6B**). We then repeated the analysis using the lead TMD
413 QTL variant (rs248974780; 155.06 Mbp) as an additive covariate (**Figure 6C**). This led
414 to the ablation of all QTLs. These results supported the presence of at least two loci
415 both driven by WSB/EiJ alleles, one influencing cortical bone morphology and Ct.Por
416 and the other influencing TMD, as well as possibly influencing cortical bone morphology
417 and Ct.Por.
418
419 ***Qsox1* is responsible for the effect of locus 1 on cortical bone morphology:**
420 Given the importance of bone morphology to strength, we sought to focus on identifying
421 the gene(s) underlying locus 1 and impacting cortical bone morphology. We re-
422 evaluated candidate genes in light of the evidence for two distinct QTL. Immediate Early

Response 5 (*Ier5)* and quiescin sulfhydryl oxidase 1 (*Qsox1*) were identified as candidates based on the DO mouse eQTL analysis and *BC034090* as a candidate based on missense variants (**Table 2**). Interestingly, *Ier5* and *Qsox1* eQTL colocalized with all QTL, except the TMD QTL, where only *Ier5* colocalized, providing additional support for two distinct loci (**Table 2 and Figure 7A**). We cannot exclude the involvement of the missense variants in *BC034090*; however, without direct evidence that they impacted *BC034090* function, we put more emphasis on the eQTL. As a result, based on its colocalizing eQTL and known biological function (see below), we predicted that *Qsox1* was at least partially responsible for locus 1.

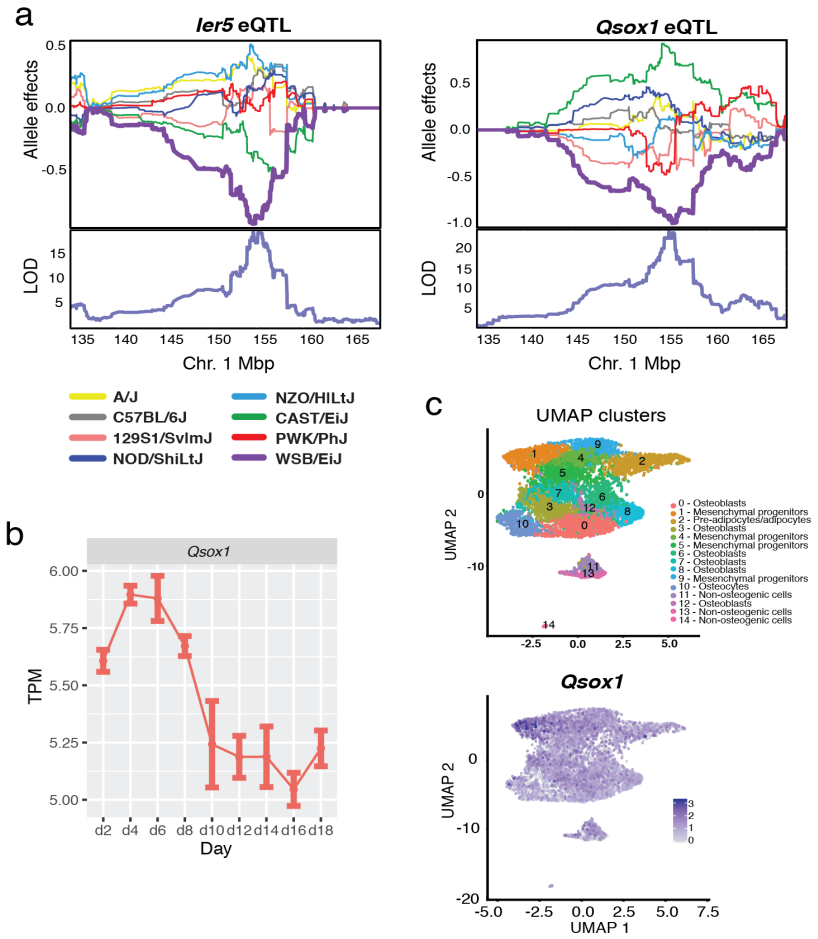

Figure 7. Characterization of *Qsox1*. a) The top panel shows allele effects for the DO founders for *Ier5* and *Qsox1* expression an interval on chromosome 1 (Mbp, colors correspond to the founder allele in the legend). Y-axis units are best linear unbiased predictors (BLUPs). Bottom panels show each respective QTL scan. LOD score threshold for autosomal eQTL is 10.89 (alpha=0.05). **b**) *Qsox1* expression in calvarial osteoblasts. Error bars represent the standard error of the mean. **c**) Single cell RNA-seq expression data. Each point represents a cell. The top panel shows UMAP clusters and their corresponding cell-type. The bottom panel shows the expression of *Qsox1.*

QSOX1 is the only

446 known secreted catalyst of disulfide bond formation and a regulator of extracellular
447 matrix integrity [63]. It has not been previously linked to skeletal development. We found
448 that *Qsox1* was highly expressed in calvarial osteoblasts and its expression decreased
449 ($P=6.4 \times 10^{-6}$) during differentiation (**Figure 7B**). In scRNA-seq on bone marrow-derived
450 stromal cells exposed to osteogenic differentiation media *in vitro*, we observed *Qsox1*
451 expression in all osteogenic cells with its highest expression seen in a cluster of
452 mesenchymal progenitors defined by genes involved in skeletal development such as
453 *Grem2*, *Lmna*, and *Prrx2* (cluster 1) (**Supplemental Table 18 and Figure 7C**).
454 Additionally, in the DO cortical bone RNA-seq data, *Qsox1* was highly co-expressed
455 with many key regulators of skeletal development and osteoblast activity (*e.g.*, *Runx2*;
456 rho=0.48, $P=<2.2 \times 10^{-16}$, *Lrp5*; rho=0.41, $P=6.2 \times 10^{-9}$).

To directly test the role of *Qsox1*, we used CRISPR/Cas9 to generate *Qsox1* mutant mice. We generated five different mutant lines harboring unique mutations, including two 1-bp frameshifts, a 171-bp in-frame deletion of the QSOX1 catalytic domain, and two large deletions (756 bp and 1347 bp) spanning most of the entire first exon of *Qsox1* (**Figure 8A, Supplemental Tables 19 and 20**). All five mutations abolished QSOX1 activity in serum (**Figure 8B**). Given the uniform lack of QSOX1 activity, we combined phenotypic data from all lines to evaluate the effect of QSOX1 deficiency on bone. We hypothesized based on the

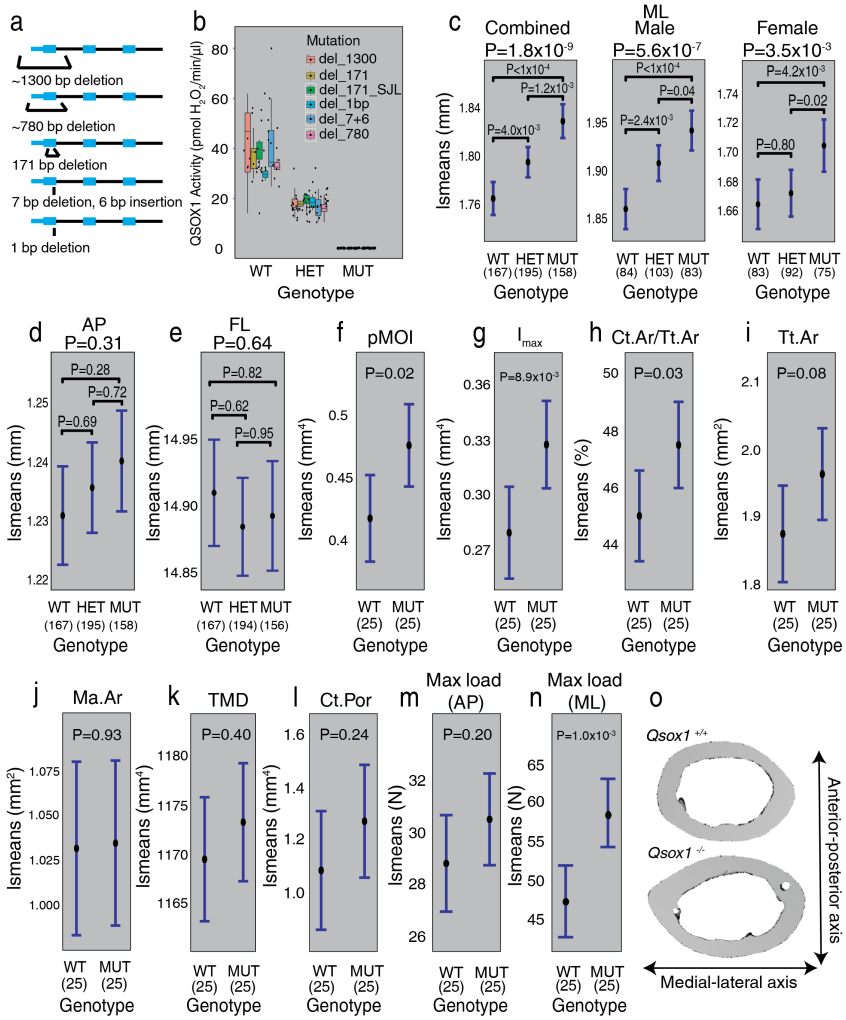

Figure 8. *Qsox1* is responsible for several chromosome 1 QTL. a) Representative image of the *Qsox1* knockout mutations. **b**) QSOX1 activity assay in serum. Data is grouped by mouse genotype. Boxplot whiskers represent 1.5 x IQR, and the center line is the median. **c-e**) Caliper-based measurements of femoral morphology in *Qsox1* mutant mice. P-values above plots are ANOVA P-values for the genotype term, while P-values in the plots are contrast P-values, adjusted for multiple comparisons. **f-l**) microCT measurements of chromosome 1 QTL phenotypes in *Qsox1* knockout mice. **m**) Bone strength (max load, F_{max}) in the AP orientation, measured via four-point bending. **n**) Bone strength (max load, F_{max}) in the ML orientation, measured via four-point bending. **o**) Representative microCT images of the effect of *Qsox1* on bone size. All error bars represent confidence intervals at a 95% confidence level.

genetic and DO mouse eQTL data, that QSOX1 deficiency would increase all traits mapping to locus 1, except TMD. Consistent with this prediction, ML was increased overall ($P=1.8 \times 10^{-9}$), and in male ($P=5.6 \times 10^{-7}$) and female ($P=3.5 \times 10^{-3}$) mice as a function of *Qsox1* mutant genotype (**Figure 8C**). Also consistent with the genetic data, we observed no difference in other gross morphological traits including anterior-posterior femoral width (AP) (P=0.31) (**Figure 8D**) and femoral length (FL) (P=0.64) (**Figure 8E**). We next focused on male *Qsox1*$^{+/+}$ and *Qsox1*$^{-/-}$ mice and used microCT to measure other bone parameters. We observed increased pMOI (P=0.02) (**Figure 8F**), Imax (P=0.009) (**Figure 8G**), and Ct.Ar/Tt.Ar (P=0.031) (**Figure 8H**). Total area (Tt.Ar) (**Figure 8I**) was increased, but the difference was only suggestive (P=0.08). Marrow area (Ma.Ar, P=0.93) was not different (**Figure 8J**). We observed no change in TMD (P=0.40) (**Figure 8K**). We also observed no difference in cortical porosity (Ct.Por) (P=0.24) (**Figure 8L**).

Given the strength of locus 1 on bone morphology and its association with biomechanical strength, we were surprised the locus did not impact femoral strength. Typically, in four-point bending assays, the force is applied along the AP axis. We replicated this in femurs from *Qsox1*$^{+/+}$ and *Qsox1*$^{-/-}$ mice and saw no significant impact on strength (P=0.20) (**Figure 8M**). However, when we tested femurs by applying the force along the ML axis, we observed a significant increase in strength in *Qsox1*$^{-/-}$ femurs ($P=1.0 \times 10^{-3}$) (**Figure 8N**). Overall, these data demonstrate that absence of QSOX1 activity leads to increased cortical bone accrual specifically along the ML axis (**Figure 8O**).

503

504 **Discussion:**

505 Human GWASs for BMD have identified over 1000 loci. However, progress in causal
506 gene discovery has been slow and BMD explains only part of the variance in bone
507 strength and the risk of fracture [7]. The goal of this study was to demonstrate that
508 systems genetics in DO mice can help address these limitations. Towards this goal, we
509 used cortical bone RNA-seq data in the DO and a network-based approach to identify
510 72 genes likely causal for BMD GWAS loci. Twenty-one of the 72 were novel. We
511 provide further evidence supporting the causality of two of these genes, *SERTAD4* and
512 *GLT8D2*. Furthermore, GWAS in the DO identified 28 QTLs for a wide-range of strength
513 associated traits. From these data, *Qsox1* was identified as a novel genetic determinant
514 of cortical bone mass and strength. These data highlight the power of systems genetics
515 in the DO and demonstrate the utility of mouse genetics to inform human GWAS and
516 bone biology.

517

518 To inform BMD GWAS, we generated Bayesian networks for cortical bone and used
519 them to identify BANs. Our analysis was similar to "key driver" analyses [29–31] where the
520 focus has often been on identifying genes with strong evidence ($P_{adj}<0.05$) of playing
521 central roles in networks. In contrast, we used BAN analysis as a way to rank genes
522 based on the likelihood ($P_{nominal} \leq 0.05$) that they are involved in a biological process
523 important to bone (based on network connections to genes known to play a role in bone
524 biology). We then identified genes most likely to be responsible for BMD GWAS
525 associations by identifying BANs regulated by human eQTL that colocalize with BMD

526 GWAS loci. Together, a gene being both a BAN in a GWAS locus and having a
527 colocalizing eQTL is strong support of causality. This is supported by the observation
528 that ~71% of the 72 BANs with colocalizing eQTL were putative regulators of bone
529 traits, based on a literature review and overlap with the “known bone gene” list.
530
531 One advantage of our network approach was the ability to not only identify causal
532 genes, but use network information to predict the cell-type through which these genes
533 are likely acting. We demonstrate this idea by investigating the two novel BANs with
534 colocalizing human eQTL from the royalblue_M module. The royalblue_M module was
535 enriched in genes involved in bone formation and ossification, suggesting the module as
536 a whole and its individual members were involved in osteoblast-driven processes. This
537 prediction was supported by the role of genes in osteoblasts that were directly
538 connected to *Sertad4* and *Glt8d2*, the expression of the two genes in osteoblasts, and
539 for *Glt8d2*, its regulation of BMD *in vivo*. Little is known regarding the specific biological
540 processes that are likely impacted by *Sertad4* and *Glt8d2* in osteoblasts; however, it will
541 be possible to utilize this information in future experiments designed to investigate their
542 specific molecular functions. For example, *Sertad4* was connected to *Wnt16*, *Ror2*, and
543 *Postn* all of which play roles in various aspects of osteoblast/osteocyte function. Wnt
544 signaling is a major driver of osteoblast-mediated bone formation and skeletal
545 development [64]. Interestingly, *Wnt16* and *Ror2* play central roles in canonical (*Wnt16*)
546 and non-canonical (*Ror2* in the *Wnt5a*/*Ror2* pathway) Wnt signaling [65] and have been
547 shown to physically interact in chondrocytes [66]. *Postn* has also been shown to influence
548 Wnt signaling [66,67]. These data suggest a possible role for *Sertad4* in Wnt signaling.

549

550 Despite their clinical importance, we know little about the genetics of bone traits other
551 than BMD. Here, we set out to address this knowledge gap. Using the DO, we identified
552 28 QTL for a wide-range of complex bone traits. The QTL were mapped at high-
553 resolution, most had 95% CIs < 1 Mbp [18]. This precision, coupled with merge and eQTL
554 analyses in DO mice, allowed us to identify a small number of candidate genes for
555 many loci. Overlap of existing human BMD GWAS association and mouse loci was no
556 more than what would be expected by chance, suggesting that our approach has
557 highlighted biological processes impacting bone that are independent of those with the
558 largest effects on BMD. This new knowledge has the potential to lead to novel pathways
559 which could be targeted therapeutically to increase bone strength. Future studies
560 extending the work presented here will lead to the identification of additional genes and
561 further our understanding of genetics of a broad range of complex skeletal traits.
562

563 Using multiple approaches, we identified *Qsox1* as responsible for at least part of the
564 effect of the locus on Chr. 1 impacting bone morphology. We use the term “at least part”
565 because it is clear that the Chr. 1 locus is complex. Using ML width as a proxy for all the
566 bone morphology traits mapping to Chr. 1, the replacement of a single WSB/EiJ allele
567 was associated with an increase in ML of 0.064 mm. Based on this, if *Qsox1* was fully
568 responsible for the Chr. 1 locus we would expect at least an ML increase of 0.128 mm
569 in *Qsox1* knockout mice; however, the observed difference was 0.064 mm (50% of the
570 expected difference). This could be due to differences in the effect of *Qsox1* deletion in
571 the DO compared to the SJL x B6 background of the *Qsox1* knockout or to additional

572 QTL in Chr. 1 locus. The latter is supported by our identification of at least two QTL in
573 the region. Further work will be needed to fully dissect this locus.
574
575 Disulfide bonds are critical to the structure and function of numerous proteins [68]. Most
576 disulfide bonds are formed in the endoplasmic reticulum [69]; however, the discovery of
577 QSOX1 demonstrated that disulfide bonds in proteins can be formed extracellularly [63].
578 Ilani et al. [63] demonstrated that fibroblasts deficient in QSOX1 had a decrease in the
579 number of disulfide bonds in matrix proteins. Moreover, the matrix formed by these cells
580 was defective in supporting cell-matrix adhesion and lacked incorporation of the alpha-4
581 isoform of laminin. QSOX1 has also been associated with perturbation of the
582 extracellular matrix in the context of cancer and tumor invasiveness [70,71]. It is unclear at
583 this point how QSOX1 influences cortical bone mass; however, it likely involves
584 modulation of the extracellular matrix.
585
586 In summary, we have used a systems genetics analysis in DO mice to inform human
587 GWAS and identify novel genetic determinants for a wide-range of complex skeletal
588 traits. Through the use of multiple synergistic approaches, we have expanded our
589 understanding of the genetics of BMD and osteoporosis. This work has the potential to
590 serve as a framework for how to use the DO, and other mouse genetic reference
591 populations, to complement and inform human genetic studies of complex disease.
592

Acknowledgements:

Research reported in this publication was supported in part by the National Institute of Arthritis and Musculoskeletal and Skin Diseases of the National Institutes of Health under Award Numbers AR057759 to C.J.R., M.C.H., and C.R.F., and AR077992 to C.R.F. B.A-B was supported in part by a National Institutes of Health, Biomedical Data Sciences Training Grant (5T32LM012416). The authors acknowledge Wenhao Xu (University of Virginia) and the Genetically Engineered Mouse Models (GEMM) core and the University of Virginia Cancer Center Support Grant (CCSG) P30CA044579 from NCI for their support generating *Qsox1* mutant mice. The authors also acknowledge the Yale School of Medicine Department of Orthopaedics and Rehabilitation's Histology and Histomorphometry Laboratory for all their work. We thank Matt Vincent (The Jackson Laboratory) and Gary Churchill (The Jackson Laboratory) for developing the QTL Viewer software and Neal Magee (University of Virginia) for hosting QTL Viewer on UVA servers. We thank the IMPC for accessibility to BMD data on *Glt8d2* knockout mice (www.mousephenotype.org). The data used for the analyses described in this manuscript were obtained from the IMPC Portal on 11/5/19. The Genotype-Tissue Expression (GTEx) Project was supported by the Common Fund of the Office of the Director of the National Institutes of Health, and by NCI, NHGRI, NHLBI, NIDA, NIMH, and NINDS. The data used for the analyses described in this manuscript were obtained from the GTEx Portal on 01/15/18.

614 **Ethics declaration:** The animal protocol for the characterization of Diversity Outbred
615 mice and the generation and characterization of *Qsox1* mutant mice was approved by
616 the Institutional Animal Care and Use Committee (IACUC) at the University of Virginia.
617
618

619 **METHODS:**

620 **Diversity Outbred mouse population and tissue harvesting:** A total of 619 (315
621 males, 304 females) Diversity Outbred (J:DO, JAX stock #0039376) mice, across 11
622 generations (gens. 23-33) were procured from The Jackson Laboratory at 4 weeks of
623 age. DO mice were fed standard chow (Envigo Teklad LM-485 irradiated mouse/rat
624 sterilizable diet. Product # 7912), and were injected with calcein (30 mg/g body weight)
625 both 7 days and 1 day prior to sacrifice. Mice were weighed and fasted overnight prior
626 to sacrifice. Mice were sacrificed at approximately 12 weeks of age (median: 86 days,
627 range: 76-94 days). Immediately prior to sacrifice, mice were anesthetized with
628 isoflurane, nose-anus length was recorded and blood collected via submandibular
629 bleeding. At sacrifice, femoral morphology (length and width) was measured with digital
630 calipers (Mitoyuto American, Aurora, IL). Right femora were wrapped in PBS soaked
631 gauze and stored in PBS at -20°C. Right tibiae were stored in 70% EtOH at room
632 temperature. Left femora were flushed of bone marrow (which was snap frozen and
633 stored in liquid nitrogen, see below – Single cell RNA-seq of bone marrow stromal cells
634 exposed to osteogenic differentiation media *in vitro*) and were immediately
635 homogenized in Trizol. Homogenates were stored at -80°C. Left tibiae were stored in
636 10% neutral buffered formalin at 4°C. Tail clips were collected and stored at -80°C.
637

638 **Measurement of trabecular and cortical microarchitecture:** Right femora were
639 scanned using a 10 μm isotropic voxel size on a desktop μCT40 (Scanco Medical AG,
640 Brüttisellen, Switzerland), following the Journal of Bone and Mineral Research
641 guidelines for assessment of bone microstructure in rodents [72]. Trabecular bone

642 architecture was analyzed in the endocortical region of the distal metaphysis. Variables
643 computed for trabecular bone regions include: bone volume, BV/TV, trabecular number,
644 thickness, separation, connectivity density and the structure model index, a measure of
645 the plate versus rod-like nature of trabecular architecture. For cortical bone at the
646 femoral midshaft, total cross-sectional area, cortical bone area, medullary area, cortical
647 thickness, cortical porosity and area moments of inertia about principal axes were
648 computed.
649
650 **Biomechanical testing:** The right femur from each mouse was loaded to failure in four-
651 point bending in the anterior to posterior direction, such that the posterior quadrant is
652 subjected to tensile loads. The widths of the lower and upper supports of the four-point
653 bending apparatus are 7 mm and 3 mm, respectively. Tests were conducted with a
654 deflection rate of 0.05 mm/s using a servohydraulic materials test system (Instron Corp.,
655 Norwood, MA). The load and mid-span deflection were acquired directly at a sampling
656 frequency of 200 Hz. Load-deflection curves were analyzed for strength (maximum
657 load), stiffness (the slope of the initial portion of the curve), post-yield deflection, and
658 total work. Post-yield deflection, which is a measure of ductility, is defined as the
659 deflection at failure minus the deflection at yield. Yield is defined as a 10% reduction of
660 stiffness relative to the initial (tangent) stiffness. Work, which is a measure of
661 toughness, is defined as the area under the load-deflection curve. Femora were tested
662 at room temperature and kept moist with phosphate buffered saline during all tests.
663

664 **Assessment of bone marrow adipose tissue (MAT):** Fixed right tibiae, dissected free
665 of soft tissues, were decalcified in EDTA for 20 days, changing the EDTA every 3-4
666 days and stained for lipid using a 1:1 mixture of 2% aqueous osmium tetroxide (OsO_4)
667 and 5% potassium dichromate. Decalcified bones were imaged using μCT performed in
668 water with energy of 55 kVp, an integration time of 500 ms, and a maximum isometric
669 voxel size of 10 μm (the "high" resolution setting with a 20mm sample holder) using a
670 μCT35 (Scanco). To determine the position of the MAT within the medullary canal and
671 to determine its change in volume, the bone was overlaid. MAT was recorded in 4
672 dimensions.
673
674 **Histomorphometry:** Fixed right tibiae were sequentially dehydrated and infiltrated in
675 graded steps with methyl methacrylate. Blocks were faced and 5 μm non-decalcified
676 sections cut and stained with toludine blue to observe gross histology. This staining
677 allows for the observation of osteoblast and osteoclast numbers, amount of
678 unmineralized osteoid and the presence of mineralized bone. Histomorphometric
679 parameters were analyzed on a computerized tablet using Osteomeasure software
680 (Osteometrics, Atlanta, GA). Histomorphometric measurements were made on a fixed
681 region just below the growth plate corresponding to the primary spongiosa.
682
683 **Bulk RNA isolation, sequencing and quantification:** We isolated RNA from a
684 randomly chosen subset (n=192, 96/sex) of the available mice at the time (mice number
685 1-417), constrained to have an equal number of male and female mice. Total RNA was
686 isolated from marrow-depleted homogenates of the left femora, using the mirVana™

687 miRNA Isolation Kit (Life Technologies, Carlsbad, CA). Total RNA-Seq libraries were
688 constructed using Illumina TruSeq Stranded Total RNA HT sample prep kits. Samples
689 were sequenced to an average of 39 million 2 x 75 bp paired-end reads (total RNA-seq)
690 on an Illumina NextSeq500 sequencer in the University of Virginia Center for Public
691 Health Genomics Genome Sciences Laboratory (GSL). A custom bioinformatics
692 pipeline was used to quantify RNA-seq data. Briefly, RNA-seq FASTQ files were quality
693 controlled using FASTQC [73], aligned to the mm10 genome assembly with HISAT2 [74],
694 and quantified with Stringtie [75]. Read count information was then extracted with a
695 Python script provided by the Stringtie website (prepDE.py). Finally, we filtered our gene
696 set to include genes that had more than 6 reads, and more than 0.1 transcripts per
697 million (TPM), in more than 38 samples (20% of all samples). This filtration resulted in
698 23,648 “genes” remaining from an initial set of 53,801 “genes”. (Note that most of these
699 “genes” were defined by StringTie internally as “genes”, but indicate loci – contiguous
700 regions on the genome where the exons of transcripts overlap). Sequencing data is
701 available on GEO (GSE152708).
702
703 **Bulk RNA differential expression analyses:**
704 RNA-seq data were subjected to a variance stabilizing transformation using the DESeq2
705 R package[76], and the 500 most variable genes were used to calculate the principal
706 components using the “PCA” function from the FactoMineR R package[77]. For
707 visualization, age was binarized into “high” and “low”, with “low” defined as age equal to,
708 or less than, the median age at sacrifice (85 days) and “high” defined as age higher
709 than 85 days. Differential expression was then performed using DESeq2, for both sex

710 and bone strength (max load). For differential expression based on sex, we used a
711 design formula of ~batch+age+sex. For bone strength, we binarized bone strength into
712 “high” and “low” for each sex independently, using the median bone strength value for
713 each sex (35.66 and 37.42 for males and females, respectively). Differential expression
714 was performed using the following design formula: ~sex+batch+age+bone strength.
715 Log2 fold changes for both differential expression analyses were then shrunken using
716 the lfcShrink() function in DESeq2, using the adaptive t prior shrinkage estimator from
717 the “apeglm” R package[78].
718
719 **Mouse genotyping:** DNA was collected from mouse tails from all 619 DO mice, using
720 the PureLink Genomic DNA mini kit (Invitrogen)**.** DNA was used for genotyping with the
721 GigaMUGA array [19] by Neogen Genomics (GeneSeek; Lincoln, NE). Genotyping reports
722 were pre-processed for use with the qtl2 R package [79] [80] , and genotypes were encoded
723 using directions and scripts from (kbroman.org/qtl2/pages/prep_do_data.html). Quality
724 control was performed using the Argyle R package [81], where samples were filtered to
725 contain no more than 5% no calls and 50% heterozygous calls. Samples that failed QC
726 were re-genotyped. Furthermore, genotyping markers were filtered to contain only tier 1
727 and tier 2 markers. Markers that did not uniquely map to the genome were also
728 removed. Finally, a qualitative threshold for the maximum number of no calls and a
729 minimum number of homozygous calls was used to filter markers.

730 We calculated genotype and allele probabilities, as well as kinship matrices using the
731 qtl2 R package. Genotype probabilities were calculated using a hidden Markov model
732 with an assumed genotyping error probability of 0.002, using the Carter-Falconer map

733 function. Genotype probabilities were then reduced to allele probabilities, and allele
734 probabilities were used to calculate kinship matrices, using the “leave one chromosome
735 out” (LOCO) parameter. Kinship matrices were also calculated using the “overall”
736 parameter for heritability calculations.

737 Further quality control was then performed [82], which led to the removal of several
738 hundred more markers that had greater than 5% genotyping errors, after which
739 genotype and allele probabilities and kinship matrices were recalculated. After the
740 aforementioned successive marker filtration, 109,427 markers remained, out of 143,259
741 initial genotyping markers. As another metric for quality control, we calculated the
742 frequencies of the eight founder genotypes of the DO.
743

744 **WGCNA network construction:** Gene counts, as obtained above were pruned to
745 remove genes that had fewer than 10 reads in more than 90% of samples. Genes not
746 located on the autosomes or X chromosome were also removed. This led to the
747 retention of 23,335 out of 23,648 genes. Variance-stabilizing transformation (DeSeq2 [76])
748 was applied, followed by RNA-seq batch correction using sex and age at sacrifice in
749 days as covariates (sex was not included as a covariate in the sex-specific networks),
750 using ComBat (“sva” R package [83]). We then used the “WGCNA” R package to generate
751 signed co-expression networks with a soft thresholding power of 4 (power=5 for male
752 networks) [84,85]. We used the “blockwiseModules” function to construct networks with a
753 merge cut height of 0.15 and minimum module size of 30. WGCNA networks had 39, 45
754 and 40 modules for the sex-combined, female and male networks, respectively.

755 **Bayesian network learning**: Bayesian networks for each WGCNA module were
756 learned with the "bnlearn" R package [86]. Specifically, expression data for genes within a
757 WGCNA module were obtained as above (WGCNA network construction), and these
758 data were used to learn the structure of the underlying Bayesian network using the Max-
759 Min Hill Climbing algorithm (function "mmhc" in bnlearn).

760 **Construction of the "known bone gene" list:** We constructed a list of bone genes
761 using Gene Ontology (GO) terms and the Mouse Genome Informatics (MGI) database [87]
762 [88]. Using AmiGO2, we downloaded GO terms for "osteo*", "bone" and "ossif*", using all
763 three GO domains (cellular component, biological process and molecular function),
764 without consideration of GO evidence codes [89]. The resulting GO terms were pruned to
765 remove some terms that were not related to bone function or regulation. We then used
766 the MGI Human and Mouse Homology data table to convert human genes to their
767 mouse homologs. We also downloaded human and mouse genes which had the terms
768 "osteoporosis", "bone mineral density", "osteoblast", "osteoclast", and "osteocyte", from
769 MGI's Human – Mouse: Disease Connection (HMDC) database. Human genes were
770 converted to their mouse counterparts as above. GO and MGI derived genes were
771 merged and duplicates were removed. Finally, we removed genes that were not
772 expressed in our dataset. That is to say, they were not considered in generating the
773 WGCNA modules or Bayesian networks.

774 **Bone Associated Node (BAN) analysis:** We used a custom script that utilized the
775 "igraph" R package to perform BAN analysis [90]. Briefly, within a Bayesian network
776 underlying a WGCNA module, we counted the number of neighbors for each gene,
777 based on a neighborhood step size of 3. Neighborhood sizes also included the gene

778 itself. BANs were defined as genes that were more highly connected to bone genes
779 than would be expected by chance. We merged all genes from all Bayesian networks
780 together in a matrix, and removed genes that were unconnected or only connected to 1
781 neighbor (neighborhood size <=2). We then pruned all genes whose neighborhood size
782 was greater than 1 standard deviation less than the mean neighborhood size across all
783 modules. These pruning steps resulted in 15,546/17,264, 13,328/16,446 and
784 13,541/17,402 genes remaining for the full, male and female Bayesian networks,
785 respectively.

786 Then, for each gene, we calculated if they were more connected to bone genes in our
787 bone list (see construction of bone list above) than expected by chance using the
788 hypergeometric distribution (phyper, R "stats" package). The arguments were as
789 follows: q: (number of genes in neighborhood that are also bone genes) – 1; m: total
790 number of bone genes in our bone gene set; n: (number of genes in networks prior to
791 pruning) – m; k: neighborhood size of the respective gene; lower.tail = false. False
792 discovery rates were calculated using p.adjust().

793 **GWAS-eQTL colocalization:** We converted mouse genes with evidence of being a
794 BAN (P<=0.05) to their human homologs using the MGI homolog data table. If the
795 human homolog was within 1Mbp of a GWAS association, we obtained all eQTL
796 associations within +/- 200 kb of the GWAS association in all 48 tissues of version 7 of
797 the Gene-Tissue Expression Project (GTEx). These eQTL variants were colocalized
798 with the GWAS variants, using the R "coloc" package, using the coloc.abf() function [91].
799 This returned posterior probabilities (PP) for five hypotheses:
800 - H0: No association with either trait.

801 - H1: Association with trait 1, not with trait 2.

802 - H2: Association with trait 2, not with trait 1.

803 - H3: Association with traits 1 and 2, two independent SNPs.

804 - H4: Association with traits 1 and 2, one shared SNP.

805 Genes were considered colocalizing if PPH4 >= 0.75.

806

807 **Gene ontology:** Gene ontology analysis for WGCNA modules was performed for each
808 individual module using the "topGO" package in R [92]. Enrichment tests were performed
809 for the "Molecular Function", "Biological Process" and "Cellular Component" ontologies,
810 using all genes in the network. Enrichment was performed using the "classic" algorithm
811 with Fisher's exact test. P-values were not corrected for multiple testing.

812 **Assessing the expression of *Glt8d2* and *Sertad4* in publicly available bone cell**
813 **data:** We used bioGPS expression data from GEO (GSE10246) to assay the
814 expression of *Sertad4*, *Glt8d2,* and *Qsox1* in osteoblasts and osteoclasts[50]. We also
815 downloaded the data from GEO (GSE54461) to query expression in primary calvarial
816 osteoblasts.

817 **Analysis of BMD data on *Glt8d2*$^{-/-}$ mice from the IMPC:** The International Mouse
818 Knockout Consortium [60] and the IMPC[93] have generated and phenotyped mice
819 harboring null alleles for *Glt8d2* (*Glt8d2*$^{tm1a(KOMP)Wtsi}$*,Glt8d2*$^{-/-}$) (N=7 females and N=7
820 males). Phenotypes for the appropriate controls (C57BL/6) were also collected
821 (N=1,466 females and N=1,477 males). A description of the battery of phenotypes
822 collected on mutants can be found at
823 (https://www.mousephenotype.org/impress/PipelineInfo?id=4). The mice were 14

824 weeks of age at DEXA scanning and both sexes were included. We downloaded raw
825 BMD, body weight and metadata for *Glt8d2* mutants from the IMPC webportal
826 (http://www.mousephenotype.org). These data were analyzed using the PhenStat R
827 package [94]. PhenStat was developed to analyze data generated by the IMPC in which a
828 large number of wild-type controls are phenotyped across a wide-time range in batches
829 and experimental mutant animals are tested in small groups interspersed among wild-
830 type batches. We used the Mixed Model framework in PhenStat to analyze BMD data.
831 The mixed model framework starts with a full model (with fixed effects of genotype, sex,
832 genotype x sex and weight and batch as a random effect) and ends with final reduced
833 model and genotype effect evaluation procedures [94,95].

834 **QTL mapping:** Phenotypes that notably deviated from normality were $\log_{10}$-transformed
835 (the MAT phenotypes as well as PYD and W_{py} were transformed after a constant of 1
836 was added). Then, QTL mapping with a single-QTL model was performed via a linear
837 mixed model using the “scan1” function of the “qtl2” R package. A kinship matrix as
838 calculated by the “leave one chromosome out” method was included. Mapping
839 covariates were sex, age at sacrifice in days, bodyweight, and DO mouse generation.
840 Peaks were then identified with a minimum LOD score of 4 and a peak drop of 1.5
841 LODs. To identify significant QTL peaks, we permuted each phenotype scan 1000 times
842 (using the “scan1perm” function of the “qtl2” package) with the same mapping
843 covariates as above, and calculated the significance threshold for each phenotype at a
844 5% significance level. Heritability for the phenotypes was calculated using the
845 “est_herit” function of the “qtl2” R package, using the same covariates as above, but
846 with a kinship matrix that was calculated using the “overall” argument.

847 **DO eQTL mapping:** Variance stabilizing transformation was applied to gene read
848 counts from above using the "DESeq2" R package, followed by quantile-based inverse
849 Normal transformation[96]. Then, hidden determinants of gene expression were calculated
850 from these transformed counts, using Probabilistic Estimation of Expression Residuals
851 (PEER)[97]. 48 PEER factors were calculated using no intercept or covariates. Sex and
852 the 48 PEER covariates were used as mapping covariates, and eQTL mapping was
853 performed using the "scan1" function, as above. To calculate a LOD score threshold, we
854 randomly chose 50 genes and permuted them 1000 times, as above. Since all genes
855 were transformed to conform to the same distribution, we found that using 50 was
856 sufficient. Thresholds were set as the highest permuted LOD score each for autosomal
857 chromosomes and the X-chromosome (10.89 and 11.55 LODs, respectively). Finally,
858 we identified peaks as above, and defined eQTL as peaks that exceeded the LOD
859 threshold and were no more than 1Mbp away from their respective transcript's start site,
860 as defined by the Stringtie output.

861 **Merge analysis:** We performed merge analysis, a previously published approach,
862 using the SNP-association methods in the "qtl2" R package [61,80]. For each DO mouse
863 QTL or eQTL peak, we imputed all variants within the 95% confidence interval of a
864 peak, and tested each variant for association with the respective trait. This was
865 performed using the "scan1snps" function of the "qtl2" R package, with the same
866 mapping covariates for QTL or eQTL, respectively. Then, we identified "top" variants by
867 taking variants that were within 85% of the maximum SNP association's LOD score. For
868 conditional analyses using a variant, we performed the same QTL scan as above, but
869 included the genotype of the respective SNP as an additive mapping covariate,

870 encoding it as a 0, 0.5 or 1, for homozygous alternative, heterozygous or homozygous
871 reference, respectively.

872 **BMD-GWAS overlap:** To identify BMD GWAS loci that overlapped with our DO mouse
873 associations, we defined a mouse association locus as the widest confidence interval
874 given all QTL start and end CI positions mapping to each locus. We then used the
875 UCSC liftOver tool [98] (minimum ratio of bases that must remap = 0.1, minimum hit size
876 in query = 100000) to convert the loci from mm10 to their syntenic hg19 positions. We
877 then took all genome-wide significant SNPs ($P <= 5 \times 10^{-8}$) from the Morris *et al.* GWAS
878 for eBMD and the Estrada *et al.* GWAS for FNBMD and LSBMD, and identified variants
879 that overlapped with the syntenic mouse loci ("GenomicRanges" R package [99]).

880 **SIFT annotations:** SIFT annotations for merge analysis missense variants were
881 queried using Ensembl's Variant Effect Predictor tool
882 (https://useast.ensembl.org/Tools/VEP) [100]. All options were left as default.

883 **Prior ML QTL mapping:** The cohorts used for the earlier QTL mapping of ML consisted
884 of 577 Diversity Outbred mice from breeding generations G10 and G11 [62]. G10 cohort
885 mice consisted of both males and females fed a defined synthetic diet (D10001,
886 Research Diets, New Brunswick, NJ), and were euthanized and analyzed at 12–15
887 weeks of age. G11 cohort mice were all females fed a defined synthetic diet (D10001,
888 Research Diets, New Brunswick, NJ) until 6 weeks of age, and were then subsequently
889 fed either a high-fat, cholesterol-containing (HFC) diet (20% fat, 1.25% cholesterol, and
890 0.5% cholic acid) or a low-fat, high protein diet (5% fat and 20.3% protein) (D12109C
891 and D12083101, respectively, Research Diets, New Brunswick, NJ), and were

892 euthanized and analyzed at 24–25 weeks of age. Mice were weighed and then
893 euthanized by CO_2 asphyxiation followed by cervical dislocation. Carcasses were frozen
894 at -80°C. Subsequently, the femur was dissected and length, AP width, and ML width
895 was measured two independent times to 0.01 mm using digital calipers. Mice were
896 genotyped using the MegaMUGA SNP array (GeneSeek; Lincoln, NE) designed with
897 77,800 SNP markers, and QTL mapping was performed as above, but with the inclusion
898 of sex, diet, age and weight at sacrifice as additive covariates.

899 **Generation of *Qsox1* mutant mice:** *Qsox1* knockout mice used in this study were
900 generated using the CRISPR/Cas9 genome editing technique essentially as reported in
901 [101]. *Qsox1* knockout mice used in this study were generated using the CRISPR/Cas9
902 genome editing technique essentially as reported in [101]. Briefly, Cas9 enzyme that was
903 injected into B6SJLF2 embryos (described below) was purchased from (PNA Bio) while
904 the guide RNA (sgRNA) was designed and synthesized as follows: the 20 nucleotide
905 (nt) sequence that would be used to generate the sgRNA was chosen using the
906 CRISPR design tool developed by the Zhang lab (crispr.mit.edu). The chosen sequence
907 and its genome map position is homologous to a region in Exon 1 that is ~225 bp, 3' of
908 the translation start site and ~20bp 5' of the Exon1/Intron1 boundary (**Supplemental**
909 **Table 21**). To generate the sgRNA that would be used for injections oligonucleotides of
910 the chosen sequence, as well as the reverse complement (**Supplemental Table 21**),
911 primers 1 and 2, respectively), were synthesized such that an additional 4 nts (CACC
912 and AAAC) were added at the 5' ends of the oligonucleotides for cloning purposes.
913 These oligonucleotides were annealed to each other by combining equal molar
914 amounts, heating to 90°C for 5 min. and allowing the mixture to passively cool to room

915 temperature. The annealed oligonucleotides were combined with BbsI digested pX330
916 plasmid vector (provided by the Zhang lab through Addgene; https://www.addgene.org/)
917 and T4 DNA ligase (NEB) and subsequently used to transform Stbl3 competent bacteria
918 (Thermo Fisher) following the manufacturer's' protocols. Plasmid DNAs from selected
919 clones were sequenced from primer 3 (**Supplemental Table 21**) and DNA that
920 demonstrated accurate sequence and position of the guide were used for all
921 downstream applications. The DNA template used in the synthesis of the sgRNA was
922 the product of a PCR using the verified plasmid DNA and primers 4 and 5
923 (**Supplemental Table 21**). The sgRNA was synthesized via *in vitro* transcription (IVT)
924 by way of the MAXIscript T7 kit (Thermo Fisher) following the manufacturer's protocol.
925 sgRNAs were purified and concentrated using the RNeasy Plus Micro kit (Qiagen)
926 following the manufacturer's protocol.
927
928 B6SJLF1 female mice (Jackson Laboratory) were super-ovulated and mated with
929 B6SJLF1 males. The females were sacrificed and the fertilized eggs (B6SJLF2
930 embryos) were isolated from the oviducts. The fertilized eggs were co-injected with the
931 purified Cas9 enzyme (50 ng/µl) and sgRNA (30 ng/µl) under a Leica inverted
932 microscope equipped with Leitz micromanipulators (Leica Microsystems). Injected eggs
933 were incubated overnight in KSOM-AA medium (Millipore Sigma). Two-cell stage
934 embryos were implanted on the following day into the oviducts of pseudo pregnant ICR
935 female mice (Envigo). Pups were initially screened by PCR of tail DNA using primers 6
936 and 7 with subsequent sequencing of the resultant product from primer 8, when the
937 PCR products suggested a relatively large deletion had occurred in at least one of the

938 alleles (**Supplemental Table 17**). For those samples which indicated a small or no
939 deletion had occurred PCR of tail DNA using primers 9 and 10 was performed with
940 subsequent sequencing of the resultant products from primer 11 (**Supplemental Table**
941 **21**). Finally, deletions were fully characterized by ligating, with T4 DNA ligase (NEB),
942 the PCR products from either primer pairs 6/7 or 9/10 with the plasmid vector pCR 2.1
943 (Thermo Fisher) followed by transformation of One Shot Top 10 chemically competent
944 cells (Thermo Fisher) following the manufacturers recommendations (**Supplemental**
945 **Tables 19 and 20**).

946 The resulting founder mice (see **Supplemental Table 19**) were mated to C57BL/6J
947 mice (Jackson Laboratory), with CRISPR/Cas9-deletion heterozygous F1 offspring from
948 the 1st and 2nd litters mated to generate the F2 offspring used in the study of bone
949 related properties reported herein. In addition, mouse B (**Supplemental Table 19**) was
950 subsequently mated to an SJL/J male (Jackson Laboratory), and the F2 offspring from
951 the heterozygous F1 crosses, as outlined above, were also used in this study. All F1
952 and F2 mice from all deletion 'strains' were genotyped using primer pairs 9/10, with the
953 PCR products sequenced from primer 11 for mice possessing the 7+6 and 1bp
954 deletions (**Supplemental Table 21**). An additional PCR using primers 6 and 7 was
955 performed with tail DNA from mice carrying the 1347 bp and 756 bp deletions; the
956 products from this 2nd PCR assisted in determining between heterozygous and
957 homozygous deleted genotypes (**Supplemental Table 21**).

958 ML was measured for both femurs using calipers on a population of 12-week old F2
959 mice and ML was averaged between the two femurs. A linear model with genotype,
960 mutation type, length, and weight was generated separately for males and females. For

961 the sex-combined data, a sex term was also included in the model. ANOVAs were
962 performed using the Anova() function from the “car” R package [102]. Lsmeans were
963 calculated using the “emmeans” R package [103]. The same procedure was performed for
964 the AP and FL sex-combined data.

965 We randomly selected 50 male F2 mice (25 wt + 25 mut) from the same population, and
966 microarchitectural phenotypes were measured as above, but on left femurs. Bone
967 strength was measured as above but in both the AP and ML orientations. A linear model
968 with genotype, mutation type and weight was generated, and lsmeans were calculated
969 using the “emmeans” R package [103].

970 **Measuring Qsox1 activity in serum:** Serum was collected via submandibular bleeding
971 from isoflurane anesthetized mice, prior to sacrifice and isolation of femurs for bone trait
972 analysis. Blood samples were incubated at room temperature for 20-30 m followed by
973 centrifugation at 2000 x g for 10 m at 4°C. The supernatants were transferred to fresh
974 tubes and centrifuged again as described above. The 2nd supernatant of each sample
975 was separated into 50-100 µl aliquots, snap frozen on dry ice and stored at -70°C. Only
976 ‘clear’ serum samples were used for determining QSOX1 activity, because pink-red
977 colored samples had slight-moderate activity, presumably due to sulfhydryl oxidase
978 enzymes released from lysed red blood cells.
979

980 Sulfhydryl oxidase activity was determined as outlined in Israel *et al.*, 2014 [104] with minor
981 modifications. Briefly, serum samples were thawed on wet ice whereupon 5 µl was
982 used in a 200 µl final reaction volume which consisted of 50 mM KPO_4, pH7.5, 1mM
983 EDTA (both from Sigma), 10 µM Amplex UltraRed (Thermo Fisher), 0.5% (v/v) Tween

984 80 (Surfact-Amps, low peroxide; Thermo Fisher), 50 nM Horseradish Peroxide (Sigma),
985 and initiated with the addition of dithiothreitol (Sigma) to 50 μM initial concentration.
986 The reactions were monitored with the 'high-sensitive dsDNA channel' of a Qubit
987 Fluorimeter (Thermo Fisher) by measuring the fluorescence every 15-30s for 10m. The
988 assay was calibrated by adding varying concentrations (0-3.2 μM) of freshly diluted
989 H_2O_2 (Sigma) to the reaction mixture minus serum. Enzyme activity was expressed in
990 units of (pmol H_2O_2/min/μl serum) and typically calculated within the first several
991 minutes of the reaction for wild-type and heterozygous mutant mice. It was calculated
992 using the entire 10m of the reaction for homozygous mutant genotypes.
993
994 **Single cell RNA-seq of bone marrow stromal cells exposed to osteogenic**
995 **differentiation media *in vitro*:**
996 *Bone marrow isolation*: The left femur was isolated and cleaned thoroughly of all muscle
997 tissue followed by removal of its distal epiphysis. The marrow was exuded by
998 centrifugation at 2000 x g for 30 seconds into a sterile tube containing 35 μl freezing
999 media (90% FBS, 10% DMSO). The marrow was then triturated 6 times on ice after
1000 addition of 150 μl ice cold freezing media and again after further addition of 1ml ice cold
1001 freezing media until no visible clumps remained prior to being placed into a Mr. Frosty
1002 Freezing Container (Thermo Scientific) and stored overnight at -80° C. Samples were
1003 transferred the following day to liquid nitrogen for long term storage.
1004
1005 *Bone marrow culturing:* Previously frozen bone marrow samples from 5 DO mice
1006 (mouse IDs: 12, 45, 48, 50, and 84) were thawed at 37° C, resuspended into 5 ml bone

1007 marrow growth media (Alpha MEM, 10% FBS, 1% Pen/Strep, 0.01% Glutamax),
1008 pelleted in a Sorvall tabletop centrifuge at 1000 rpm for 5 minutes at room temperature
1009 and then subjected to red blood cell lysis by resuspending and triturating the resultant
1010 pellet into 5 ml 0.2% NaCl for 20 seconds, followed by addition and thorough mixing of
1011 1.6% NaCl. Cells were pelleted again, resuspended into 1 ml bone marrow growth
1012 media, plated into one well per sample of a 48 well tissue culture plate and placed into a
1013 37° C, 5% CO_2 incubator undisturbed for 3 days post-plating, at which time the media
1014 was aspirated, cells were washed with 1 ml DPBS once and bone marrow growth media
1015 was replaced at 300 µl volume. The process was repeated through day 5 post-plating.
1016 At day 6 post-plating, cells were washed in same manner; however, we performed a
1017 standard *in vitro* osteoblast differentiation protocol, by replacing bone marrow growth
1018 media with 300 µl osteogenic differentiation media (Alpha MEM, 10% FBS, 1% Penicillin
1019 Streptomycin, 0.01% Glutamax, 50 mg/ml Ascorbic Acid, 1M B-glycerophosphate,
1020 100µM Dexamethasome). Cells undergoing differentiation were assessed for
1021 accumulated mineralization on days 4, 6, 8 and 10 of the differentiation process as
1022 follows: IRDye 680 BoneTag Optical Probe (Li-Cor Biosciences, product #926-09374)
1023 was reconstituted according to the manufacturer's instructions. On days 3, 5, 7 and 9,
1024 0.006 nmoles were added to each sample. Twenty-four hours later the cells were
1025 washed with 0.5 mls DPBS (Gibco, product #14190250) and media was replaced. The
1026 cells were then placed on the Odyssey CLx Imaging System (Li-Cor Biosciences) to
1027 measure mineralization density as reflected by IRDye 680 BoneTag Optical Probe
1028 incorporation. Final values for mineralization were computed by subtracting the average

1029 number of fluorescent units recorded in designated background wells from the number
1030 of fluorescent units recorded in the sample wells.
1031
1032 *RNA isolation:* The isolation procedure outlined below was inspired by [105]. Mineralized
1033 cultures were washed twice with Dulbecco's Phosphate Buffered Saline (DPBS). 0.5ml
1034 60mM EDTA (pH 7.4, made in DPBS) was added for 15-minute room temperature (RT)
1035 incubation. EDTA solution was aspirated and replaced for a second 15-minute RT
1036 incubation. Cultures were then washed with 0.5ml Hank's Balanced Salt Solution
1037 (HBSS) and incubated with 0.5ml 8mg/ml collagenase in HBSS/4mM $CaCl_2$ for 10
1038 minutes at 37° C with shaking. Cultures were triturated 10x and incubated for an
1039 additional 20 minutes and 37° C. Cultures were then transferred to a 1.5ml Eppendorf
1040 tube, and spun at 500 x g for 5 minutes at RT in a Sorvall tabletop centrifuge. Cultures
1041 were resuspended in 0.5ml 0.25% trypsin-EDTA (Gibco, Gaithersburg, MD) and
1042 incubated for 15 minutes at 37° C. Cultures were then triturated and incubated for an
1043 additional 15 minutes. 0.5ml of media were added, triturated and spun at 500 x g for 5
1044 minutes at RT. Cultures were then resuspended in 0.5ml bone marrow differentiation
1045 media and cells were counted.
1046
1047 *Library preparation, sequencing and analysis:* The samples were pooled and
1048 concentrated to 800 cells/μl in sterile PBS supplemented with 0.1% BSA. The single cell
1049 suspension was loaded into a 10x Chromium Controller (10X Genomics, Pleasanton,
1050 CA, USA), aiming to capture 8,000 cells, with the Single Cell 3' v2 reagent kit, according
1051 to the manufacturer's protocol. Following GEM capturing and lysis, cDNA was amplified

1052 (13 cycles) and the manufacturer's protocol was followed to generate sequencing
1053 library. The library was sequenced on the Illumina NextSeq500 and the raw sequencing
1054 data was processed using CellRanger toolkit (version 2.0.1). The reads were mapped to
1055 mm10 mouse reference genome assembly using STAR (version 2.5.1b) [106]. Overall,
1056 7,188 cells were sequenced, to a mean depth of 57,717 reads per cell. Sequencing data
1057 is available on GEO (GSE152806).
1058
1059 Analysis was performed using Seurat [107,108]. Features detected in at least 3 cells where
1060 at least 200 features were detected were used. We then filtered out cells with less than
1061 800 reads and more than 5800 reads, as well as cells with 10% or more mitochondrial
1062 reads. This resulted in 7,092 remaining cells. Expression measurements were multiplied
1063 by 10,000 and log normalized, and the 3000 most variable features were identified. The
1064 data were then scaled. Cells were then scored by cell cycle markers, and these scores,
1065 as well as the percentage of mitochondrial reads, were regressed out [109]. Finally,
1066 clusters were found with a resolution of 1 and the UMAP was generated. An outlier
1067 cluster consisting of 13 cells was removed. Cluster cell types were manually annotated
1068 after performing differential expression analyses of the expression of genes in each
1069 cluster relative to all other clusters (**Supplemental Table 14**), using the Seurat
1070 FindAllMarkers() function, with the only.pos=TRUE argument.
1071
1072 **Data availability:**
1073 Raw genotyping data, calculated genotype and allele probabilities, and R/qtl2 cross files
1074 are available from Zenodo at DOI:10.5281/zenodo.4265417. Raw sequencing data is

available from the NCBI Gene Expression Omnibus database (GSE152708, GSE152806). Mapped DO mouse QTL and eQTL can be viewed at http://qtlviewer.uvadcos.io/.

GWAS summary statistics used for this study can be downloaded from http://www.gefos.org/?q=content/data-release-2018 and http://www.gefos.org/?q=content/data-release-2012.

Code availability:

Analysis code is available at https://github.com/basel-maher/DO_project

1086 **REFERENCES:**

1087 1. Black, D. M. & Rosen, C. J. Clinical Practice. Postmenopausal Osteoporosis. *N. Engl. J.*
1088 *Med.* **374**, 254–262 (2016).
1089 2. Burge, R. *et al.* Incidence and economic burden of osteoporosis-related fractures in the
1090 United States, 2005-2025. *J. Bone Miner. Res.* **22**, 465–475 (2007).
1091 3. Estrada, K. *et al.* Genome-wide meta-analysis identifies 56 bone mineral density loci and
1092 reveals 14 loci associated with risk of fracture. *Nat. Genet.* **44**, 491–501 (2012).
1093 4. Kemp, J. P. *et al.* Identification of 153 new loci associated with heel bone mineral density
1094 and functional involvement of GPC6 in osteoporosis. *Nat. Genet.* **49**, 1468–1475 (2017).
1095 5. Morris, J. A. *et al.* An atlas of genetic influences on osteoporosis in humans and mice. *Nat.*
1096 *Genet.* **51**, 258–266 (2019).
1097 6. Richards, J. B., Zheng, H.-F. & Spector, T. D. Genetics of osteoporosis from genome-wide
1098 association studies: advances and challenges. *Nat. Rev. Genet.* **13**, 576–588 (2012).
1099 7. Sabik, O. L. & Farber, C. R. Using GWAS to identify novel therapeutic targets for
1100 osteoporosis. *Transl. Res.* **181**, 15–26 (2017).
1101 8. Nadeau, J. H. & Dudley, A. M. Genetics. Systems genetics. *Science* **331**, 1015–1016
1102 (2011).
1103 9. Civelek, M. & Lusis, A. J. Systems genetics approaches to understand complex traits. *Nat.*
1104 *Rev. Genet.* **15**, 34–48 (2014).
1105 10. GTEx Consortium *et al.* Genetic effects on gene expression across human tissues. *Nature*
1106 **550**, 204–213 (2017).
1107 11. Al-Barghouthi, B. M. & Farber, C. R. Dissecting the Genetics of Osteoporosis using
1108 Systems Approaches. *Trends Genet.* **35**, 55–67 (2019).
1109 12. Dufresne, T. E., Chmielewski, P. A., Manhart, M. D., Johnson, T. D. & Borah, B.
1110 Risedronate preserves bone architecture in early postmenopausal women in 1 year as
1111 measured by three-dimensional microcomputed tomography. *Calcif. Tissue Int.* **73**, 423–

432 (2003).

13. Cummings, S. R. *et al.* Improvement in spine bone density and reduction in risk of vertebral fractures during treatment with antiresorptive drugs. *Am. J. Med.* **112**, 281–289 (2002).
14. Lochmüller, E.-M. *et al.* Correlation of Femoral and Lumbar DXA and Calcaneal Ultrasound, Measured In Situ with Intact Soft Tissues, with the In Vitro Failure Loads of the Proximal Femur. *Osteoporosis International* vol. 8 591–598 (1998).
15. Melton, L. J., III, Chrischilles, E. A., Cooper, C., Lane, A. W. & Riggs, B. L. How Many Women Have Osteoporosis? *J. Bone Miner. Res.* **20**, 886–892 (2005).
16. Churchill, G. A., Gatti, D. M., Munger, S. C. & Svenson, K. L. The Diversity Outbred mouse population. *Mamm. Genome* **23**, 713–718 (2012).
17. Logan, R. W., Robledo, R. F. & Recla, J. M. High-precision genetic mapping of behavioral traits in the diversity outbred mouse population. *Genes Brain Behav.* (2013).
18. Svenson, K. L. *et al.* High-resolution genetic mapping using the Mouse Diversity outbred population. *Genetics* **190**, 437–447 (2012).
19. Morgan, A. P. *et al.* The Mouse Universal Genotyping Array: From Substrains to Subspecies. *G3* **6**, 263–279 (2015).
20. Karasik, D. *et al.* Heritability and Genetic Correlations for Bone Microarchitecture: The Framingham Study Families. *J. Bone Miner. Res.* **32**, 106–114 (2017).
21. Ng, A. H. M., Wang, S. X., Turner, C. H., Beamer, W. G. & Grynpas, M. D. Bone quality and bone strength in BXH recombinant inbred mice. *Calcif. Tissue Int.* **81**, 215–223 (2007).
22. Turner, C. H. *et al.* Variation in bone biomechanical properties, microstructure, and density in BXH recombinant inbred mice. *J. Bone Miner. Res.* **16**, 206–213 (2001).
23. Schlecht, S. H. & Jepsen, K. J. Functional integration of skeletal traits: an intraskeletal assessment of bone size, mineralization, and volume covariance. *Bone* **56**, 127–138 (2013).
24. Szweras, M. *et al.* alpha 2-HS glycoprotein/fetuin, a transforming growth factor-beta/bone

1138 morphogenetic protein antagonist, regulates postnatal bone growth and remodeling. *J. Biol.*
1139 *Chem.* **277**, 19991–19997 (2002).
1140 25. Yeon, J.-T., Choi, S.-W. & Kim, S. H. Arginase 1 is a negative regulator of osteoclast
1141 differentiation. *Amino Acids* **48**, 559–565 (2016).
1142 26. Calabrese, G. M. *et al.* Integrating GWAS and Co-expression Network Data Identifies Bone
1143 Mineral Density Genes SPTBN1 and MARK3 and an Osteoblast Functional Module. *Cell*
1144 *Syst* **4**, 46-59.e4 (2017).
1145 27. Sabik, O. L., Calabrese, G. M., Taleghani, E., Ackert-Bicknell, C. L. & Farber, C. R.
1146 Identification of a core module for bone mineral density through the integration of a co-
1147 expression network and GWAS data. *Cell Rep.* **32**, 108145 (2020).
1148 28. Zhang, B. & Horvath, S. A general framework for weighted gene co-expression network
1149 analysis. *Stat. Appl. Genet. Mol. Biol.* **4**, Article17 (2005).
1150 29. Watson, C. T. *et al.* Integrative transcriptomic analysis reveals key drivers of acute peanut
1151 allergic reactions. *Nat. Commun.* **8**, 1943 (2017).
1152 30. Huan, T. *et al.* Integrative network analysis reveals molecular mechanisms of blood
1153 pressure regulation. *Mol. Syst. Biol.* **11**, 799 (2015).
1154 31. Wang, I.-M. *et al.* Systems analysis of eleven rodent disease models reveals an
1155 inflammatome signature and key drivers. *Mol. Syst. Biol.* **8**, 594 (2012).
1156 32. Mäkinen, V.-P. *et al.* Integrative genomics reveals novel molecular pathways and gene
1157 networks for coronary artery disease. *PLoS Genet.* **10**, e1004502 (2014).
1158 33. Aguet, F. *et al.* The GTEx Consortium atlas of genetic regulatory effects across human
1159 tissues. *bioRxiv* 787903 (2019) doi:10.1101/787903.
1160 34. Aguet, F. *et al.* Local genetic effects on gene expression across 44 human tissues. *bioRxiv*
1161 074450 (2016) doi:10.1101/074450.
1162 35. GTEx Consortium. The GTEx Consortium atlas of genetic regulatory effects across human
1163 tissues. *Science* **369**, 1318–1330 (2020).

1164 36. Nakashima, K. *et al.* The novel zinc finger-containing transcription factor osterix is required
1165 for osteoblast differentiation and bone formation. *Cell* **108**, 17–29 (2002).
1166 37. Balemans, W. *et al.* Increased bone density in sclerosteosis is due to the deficiency of a
1167 novel secreted protein (SOST). *Hum. Mol. Genet.* **10**, 537–543 (2001).
1168 38. Brunkow, M. E. *et al.* Bone dysplasia sclerosteosis results from loss of the SOST gene
1169 product, a novel cystine knot-containing protein. *Am. J. Hum. Genet.* **68**, 577–589 (2001).
1170 39. Gong, Y. *et al.* LDL receptor-related protein 5 (LRP5) affects bone accrual and eye
1171 development. *Cell* **107**, 513–523 (2001).
1172 40. Little, R. D. *et al.* A mutation in the LDL receptor-related protein 5 gene results in the
1173 autosomal dominant high-bone-mass trait. *Am. J. Hum. Genet.* **70**, 11–19 (2002).
1174 41. Boyden, L. M. *et al.* High bone density due to a mutation in LDL-receptor-related protein 5.
1175 *N. Engl. J. Med.* **346**, 1513–1521 (2002).
1176 42. Kong, Y. Y. *et al.* OPGL is a key regulator of osteoclastogenesis, lymphocyte development
1177 and lymph-node organogenesis. *Nature* **397**, 315–323 (1999).
1178 43. Wong, B. R. *et al.* TRANCE (Tumor Necrosis Factor [TNF]-related Activation-induced
1179 Cytokine), a New TNF Family Member Predominantly Expressed in T cells, Is a Dendritic
1180 Cell–specific Survival Factor. *Journal of Experimental Medicine* vol. 186 2075–2080 (1997).
1181 44. Yasuda, H. *et al.* Osteoclast differentiation factor is a ligand for
1182 osteoprotegerin/osteoclastogenesis-inhibitory factor and is identical to TRANCE/RANKL.
1183 *Proc. Natl. Acad. Sci. U. S. A.* **95**, 3597–3602 (1998).
1184 45. Lacey, D. L. *et al.* Osteoprotegerin ligand is a cytokine that regulates osteoclast
1185 differentiation and activation. *Cell* **93**, 165–176 (1998).
1186 46. Anderson, D. M. *et al.* A homologue of the TNF receptor and its ligand enhance T-cell
1187 growth and dendritic-cell function. *Nature* **390**, 175–179 (1997).
1188 47. Wong, B. R. *et al.* The TRAF family of signal transducers mediates NF-kappaB activation
1189 by the TRANCE receptor. *J. Biol. Chem.* **273**, 28355–28359 (1998).

1190 48. Wu, J., Glimcher, L. H. & Aliprantis, A. O. HCO3-/Cl- anion exchanger SLC4A2 is required
1191 for proper osteoclast differentiation and function. *Proc. Natl. Acad. Sci. U. S. A.* **105**,
1192 16934–16939 (2008).
1193 49. Duan, X., Yang, S., Zhang, L. & Yang, T. V-ATPases and osteoclasts: ambiguous future of
1194 V-ATPases inhibitors in osteoporosis. *Theranostics* **8**, 5379–5399 (2018).
1195 50. Lattin, J. E. *et al.* Expression analysis of G Protein-Coupled Receptors in mouse
1196 macrophages. *Immunome Res.* **4**, 5 (2008).
1197 51. Bennetts, J. S. *et al.* Evolutionary conservation and murine embryonic expression of the
1198 gene encoding the SERTA domain-containing protein CDCA4 (HEPP). *Gene* **374**, 153–165
1199 (2006).
1200 52. Zhan, Y. *et al.* Mechanism of the effect of glycosyltransferase GLT8D2 on fatty liver. *Lipids*
1201 *Health Dis.* **14**, 43 (2015).
1202 53. Movérare-Skrtic, S. *et al.* Osteoblast-derived WNT16 represses osteoclastogenesis and
1203 prevents cortical bone fragility fractures. *Nat. Med.* **20**, 1279–1288 (2014).
1204 54. Takeshita, S., Kikuno, R., Tezuka, K. & Amann, E. Osteoblast-specific factor 2: cloning of a
1205 putative bone adhesion protein with homology with the insect protein fasciclin I. *Biochem. J*
1206 **294 (Pt 1)**, 271–278 (1993).
1207 55. Horiuchi, K. *et al.* Identification and characterization of a novel protein, periostin, with
1208 restricted expression to periosteum and periodontal ligament and increased expression by
1209 transforming growth factor beta. *J. Bone Miner. Res.* **14**, 1239–1249 (1999).
1210 56. Izu, Y., Ezura, Y., Koch, M., Birk, D. E. & Noda, M. Collagens VI and XII form complexes
1211 mediating osteoblast interactions during osteogenesis. *Cell Tissue Res.* **364**, 623–635
1212 (2016).
1213 57. Amiri, N. & Christians, J. K. PAPP-A2 expression by osteoblasts is required for normal
1214 postnatal growth in mice. *Growth Horm. IGF Res.* **25**, 274–280 (2015).
1215 58. Wilm, B., Dahl, E., Peters, H., Balling, R. & Imai, K. Targeted disruption of Pax1 defines its

1216 null phenotype and proves haploinsufficiency. *Proc. Natl. Acad. Sci. U. S. A.* **95**, 8692–
1217 8697 (1998).
1218 59. Kimura, H., Akiyama, H., Nakamura, T. & de Crombrugghe, B. Tenascin-W inhibits
1219 proliferation and differentiation of preosteoblasts during endochondral bone formation.
1220 *Biochem. Biophys. Res. Commun.* **356**, 935–941 (2007).
1221 60. Koscielny, G. *et al.* The International Mouse Phenotyping Consortium Web Portal, a unified
1222 point of access for knockout mice and related phenotyping data. *Nucleic Acids Res.* **42**,
1223 D802-9 (2014).
1224 61. Yalcin, B., Flint, J. & Mott, R. Using Progenitor Strain Information to Identify Quantitative
1225 Trait Nucleotides in Outbred Mice. *Genetics* vol. 171 673–681 (2005).
1226 62. Shorter, J. R. *et al.* Quantitative trait mapping in Diversity Outbred mice identifies two
1227 genomic regions associated with heart size. *Mamm. Genome* **29**, 80–89 (2018).
1228 63. Ilani, T. *et al.* A secreted disulfide catalyst controls extracellular matrix composition and
1229 function. *Science* **341**, 74–76 (2013).
1230 64. Huybrechts, Y., Mortier, G., Boudin, E. & Van Hul, W. WNT Signaling and Bone: Lessons
1231 From Skeletal Dysplasias and Disorders. *Front. Endocrinol.* **11**, 165 (2020).
1232 65. Teufel, S. & Hartmann, C. Wnt-signaling in skeletal development. *Curr. Top. Dev. Biol.* **133**,
1233 235–279 (2019).
1234 66. Tong, W. *et al.* Wnt16 attenuates osteoarthritis progression through a PCP/JNK-mTORC1-
1235 PTHrP cascade. *Ann. Rheum. Dis.* **78**, 551–561 (2019).
1236 67. Bonnet, N., Garnero, P. & Ferrari, S. Periostin action in bone. *Mol. Cell. Endocrinol.* **432**,
1237 75–82 (2016).
1238 68. Rajpal, G. & Arvan, P. Chapter 236 - Disulfide Bond Formation. in *Handbook of Biologically*
1239 *Active Peptides (Second Edition)* (ed. Kastin, A. J.) 1721–1729 (Academic Press, 2013).
1240 69. Bulleid, N. J. & Ellgaard, L. Multiple ways to make disulfides. *Trends in Biochemical*
1241 *Sciences* vol. 36 485–492 (2011).

1242 70. Feldman, T. *et al.* Inhibition of fibroblast secreted QSOX1 perturbs extracellular matrix in
1243 the tumor microenvironment and decreases tumor growth and metastasis in murine cancer
1244 models. *Oncotarget* **11**, 386–398 (2020).
1245 71. Hanavan, P. D. *et al.* Ebselen inhibits QSOX1 enzymatic activity and suppresses invasion
1246 of pancreatic and renal cancer cell lines. *Oncotarget* **6**, 18418–18428 (2015).
1247 72. Bouxsein, M. L. *et al.* Guidelines for assessment of bone microstructure in rodents using
1248 micro--computed tomography. *J. Bone Miner. Res.* **25**, 1468–1486 (2010).
1249 73. Andrews, S. & Others. FastQC: a quality control tool for high throughput sequence data.
1250 (2010).
1251 74. Kim, D., Paggi, J. M., Park, C., Bennett, C. & Salzberg, S. L. Graph-based genome
1252 alignment and genotyping with HISAT2 and HISAT-genotype. *Nat. Biotechnol.* **37**, 907–915
1253 (2019).
1254 75. Pertea, M. *et al.* StringTie enables improved reconstruction of a transcriptome from RNA-
1255 seq reads. *Nat. Biotechnol.* **33**, 290–295 (2015).
1256 76. Love, M. I., Huber, W. & Anders, S. Moderated estimation of fold change and dispersion for
1257 RNA-seq data with DESeq2. *Genome Biol.* **15**, 550 (2014).
1258 77. Lê, S., Josse, J. & Husson, F. FactoMineR: AnRPackage for multivariate analysis. *J. Stat.*
1259 *Softw.* **25**, (2008).
1260 78. Zhu, A., Ibrahim, J. G. & Love, M. I. Heavy-tailed prior distributions for sequence count
1261 data: removing the noise and preserving large differences. *Bioinformatics* **35**, 2084–2092
1262 (2019).
1263 79. Team, R. C. & Others. R: A language and environment for statistical computing. (2013).
1264 80. Broman, K. W. *et al.* R/qtl2: Software for Mapping Quantitative Trait Loci with High-
1265 Dimensional Data and Multiparent Populations. *Genetics* **211**, 495–502 (2019).
1266 81. Morgan, A. P. argyle: An R Package for Analysis of Illumina Genotyping Arrays. *G3* **6**,
1267 281–286 (2015).

1268 82. Broman, K. W., Gatti, D. M., Svenson, K. L., Sen, Ś. & Churchill, G. A. Cleaning Genotype
1269 Data from Diversity Outbred Mice. *G3* **9**, 1571–1579 (2019).
1270 83. Leek, J. T., Johnson, W. E., Parker, H. S., Jaffe, A. E. & Storey, J. D. The sva package for
1271 removing batch effects and other unwanted variation in high-throughput experiments.
1272 *Bioinformatics* **28**, 882–883 (2012).
1273 84. Langfelder, P. & Horvath, S. WGCNA: an R package for weighted correlation network
1274 analysis. *BMC Bioinformatics* **9**, 559 (2008).
1275 85. Langfelder, P. & Horvath, S. Fast R Functions for Robust Correlations and Hierarchical
1276 Clustering. *J. Stat. Softw.* **46**, (2012).
1277 86. Scutari, M. Learning Bayesian Networks with thebnlearnRPackage. *Journal of Statistical*
1278 *Software* vol. 35 (2010).
1279 87. Ashburner, M. *et al.* Gene Ontology: tool for the unification of biology. *Nature Genetics* vol.
1280 25 25–29 (2000).
1281 88. Blake, J. A. *et al.* The Mouse Genome Database (MGD): premier model organism resource
1282 for mammalian genomics and genetics. *Nucleic Acids Res.* **39**, D842-8 (2011).
1283 89. Carbon, S. *et al.* AmiGO: online access to ontology and annotation data. *Bioinformatics* **25**,
1284 288–289 (2009).
1285 90. Csardi, G., Nepusz, T. & Others. The igraph software package for complex network
1286 research. *InterJournal, complex systems* **1695**, 1–9 (2006).
1287 91. Giambartolomei, C. *et al.* Bayesian Test for Colocalisation between Pairs of Genetic
1288 Association Studies Using Summary Statistics. *PLoS Genetics* vol. 10 e1004383 (2014).
1289 92. Alexa, A. Rahnenfuhrer J. topGO: enrichment analysis for Gene Ontology. 2010. *R*
1290 *package version* **2**, 45 (2017).
1291 93. Dickinson, M. E. *et al.* High-throughput discovery of novel developmental phenotypes.
1292 *Nature* **537**, 508–514 (2016).
1293 94. Kurbatova, N., Karp, N., Mason, J. & Haselimashhadi, H. PhenStat: statistical analysis of

1294 phenotypic data. *R package version* **2**, (2015).
1295 95. West, B. T., Welch, K. B. & Galecki, A. T. *Linear Mixed Models: A Practical Guide Using*
1296 *Statistical Software, Second Edition*. (CRC Press, 2014).
1297 96. Yang, J. *et al.* FTO genotype is associated with phenotypic variability of body mass index.
1298 *Nature* **490**, 267–272 (2012).
1299 97. Stegle, O., Parts, L., Piipari, M., Winn, J. & Durbin, R. Using probabilistic estimation of
1300 expression residuals (PEER) to obtain increased power and interpretability of gene
1301 expression analyses. *Nat. Protoc.* **7**, 500–507 (2012).
1302 98. Hinrichs, A. S. *et al.* The UCSC Genome Browser Database: update 2006. *Nucleic Acids*
1303 *Res.* **34**, D590-8 (2006).
1304 99. Lawrence, M. *et al.* Software for Computing and Annotating Genomic Ranges. *PLoS*
1305 *Computational Biology* vol. 9 e1003118 (2013).
1306 100. McLaren, W. *et al.* The Ensembl Variant Effect Predictor. *Genome Biol.* **17**, 122 (2016).
1307 101. Mesner, L. D. *et al.* Mouse genome-wide association and systems genetics identifies Lhfp
1308 as a regulator of bone mass. *PLoS Genet.* **15**, e1008123 (2019).
1309 102. Fox, J. & Weisberg, S. *An R companion to applied regression*. (SAGE Publications, 2018).
1310 103. Russell, L. emmeans: Estimated Marginal Means, aka Least-Squares Means. R package
1311 version 1.4. (2019).
1312 104. Israel, B. A., Jiang, L., Gannon, S. A. & Thorpe, C. Disulfide bond generation in mammalian
1313 blood serum: detection and purification of quiescin-sulfhydryl oxidase. *Free Radic. Biol.*
1314 *Med.* **69**, 129–135 (2014).
1315 105. Hanna, H., Mir, L. M. & Andre, F. M. In vitro osteoblastic differentiation of mesenchymal
1316 stem cells generates cell layers with distinct properties. *Stem Cell Res. Ther.* **9**, 203 (2018).
1317 106. Dobin, A. *et al.* STAR: ultrafast universal RNA-seq aligner. *Bioinformatics* **29**, 15–21 (2013).
1318 107. Butler, A., Hoffman, P., Smibert, P., Papalexi, E. & Satija, R. Integrating single-cell
1319 transcriptomic data across different conditions, technologies, and species. *Nat. Biotechnol.*

1320 **36**, 411–420 (2018).

1321 108. Stuart, T. *et al.* Comprehensive Integration of Single-Cell Data. *Cell* **177**, 1888-1902.e21

1322 (2019).

1323 109. Tirosh, I. *et al.* Dissecting the multicellular ecosystem of metastatic melanoma by single-cell

1324 RNA-seq. *Science* **352**, 189–196 (2016).